Rend. Lincei Mat. Appl. (Online first) DOI 10.4171/RLM/1046

© 2025 Accademia Nazionale dei Lincei Published by EMS Press



Fluid Mechanics. – Special phenomena occurring in small blood vessels: Models, interpretation and importance for life, by Angiolo Farina, Antonio Fasano and Fabio Rosso, communicated on 13 December 2024.

ABSTRACT. – This article deals with special phenomena that characterize the blood circulation in arterioles and venules (size range 50–500 µm): the Fåhræus-effect, the Fåhræus-Lindqvist effect and vasomotion. These phenomena were discovered a long time ago and have been the subject of various conjectures, both about the physical causes and the physiological effects. Some of these conjectures have turned out to be wrong, but in any case, it is confirmed that these phenomena have a fundamental importance for life. A series of studies by the present authors between 2016 and 2023 have provided a physical interpretation of such phenomena based on rigorous mathematical models. Furthermore, our analysis includes the study of the combination of vasomotion and the Fåhræus-Lindqvist effect. We emphasize how these effects influence each other and why they prove to be very important for life by enhancing venous circulation and making the process of peripheral O₂/CO₂ exchange more efficient. Particular attention will be paid to the latter aspect and the comparison of the model results with the experimental results collected over the years. The material is structured to emphasize the effectiveness of the mathematical approach and its consistency with the underlying physiology and experimental measurements.

Keywords. – hemodynamics, RBC's migration, blood microcirculation, vasomotion, perfusion.

MATHEMATICS SUBJECT CLASSIFICATION 2020. - 76Z05.

1. Introduction

Blood dynamics presents a challenging problem in physics due to the composite nature of the medium. Various techniques have been proposed to describe these phenomena, such as particle-based multiscale methods (see [11,78]). Another valuable approach is Computational Fluid Dynamics (CFD) modeling, which is particularly useful when other imaging modalities are unavailable, and in-depth flow assessment is required. CFD involves numerically solving relevant physical equations to approximate the hemodynamics of blood flow and the behavior of surrounding tissues (see, for instance, [19,31,32,66,67,71] and references therein). Additionally, dissipative particle dynamics has been used to study the complex interactions in blood flow (see [30,44]).

One of the major challenges in modeling blood flow through micro-channels arises because, at scales ranging from tens to hundreds of microns, blood behaves as a multiphase suspension of deformable particles (see [62]). For a comprehensive overview of this subject, see Bessonov et al. [7] which provides an excellent review of the peculiar characteristics of blood rheology.

One, if not the most important of these characteristics, is that blood viscosity may vary with vessel diameter, hematocrit and blood flow discharge.

Our approach to studying blood microcirculation aims to explain certain longobserved phenomena based on solid physical principles. This approach contrasts with studies that derive empirical formulas to fit experimental measurements (see, e.g., [65]). Instead, we aim to derive such formulas theoretically and then validate them with available data.

Jean-Léonard-Marie Poiseuille (1797–1869) was an outstanding personality who received an excellent scientific education at the École Polytechnique (where Ampère was one of his teachers) and went on to study medicine. No wonder he laid the foundations of hemodynamics by experimenting with blood flowing through tubes. The famous law that bears his name¹ links the flow rate² Q^* to the pressure drop Δp^* , the pipe radius R^* and the length L^* :

(1.1)
$$Q^* = \frac{\pi R^{*4}}{8n^*L^*} \Delta p^*,$$

where η^* is the viscosity of the fluid. The law, which only applies to incompressible Newtonian fluids with laminar flow, can be easily derived from the basic equations of fluid dynamics (the Navier–Stokes equation and the continuity equation). These classical equations have been extensively and successfully used to model blood flow in a sufficiently large vessel, including the so-called fluid-structure interaction, i.e. the deformability of the vessel wall (see [29, Chapter 1], for bibliographical references). Of course, more sophisticated dynamical models have been proposed for blood, based on various constitutive laws, but we can say that the basic Newtonian model works quite reasonably in many cases [1,29]. However, a completely different scenario arises when we consider "small" vessels. A sentence by Mchedlishvili [59] is worth mentioning:

The available laws of fluid mechanics cannot be used for a better understanding of the microcirculation in the living capillaries, and hemorheology in the microcirculation requires a different approach than the laws of fluid mechanics.

⁽¹⁾ The law is often referred to as the Hagen–Poiseuille law, whereby the name of the German engineer is Gotthilf Heinrich Ludwig Hagen (1797–1884), who discovered it independently.

⁽²⁾ Starred quantities are meant to be dimensional.

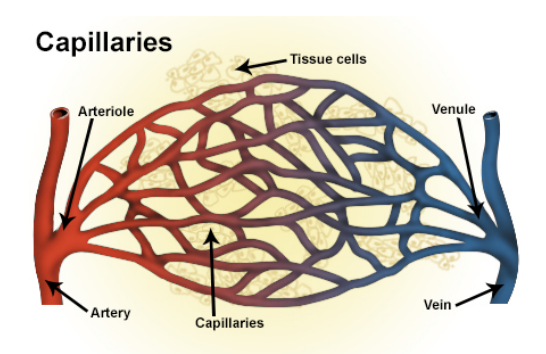


FIGURE 1. Based on their structure and function, blood vessels are classified as either arteries, capillaries or veins. Arteries carry blood away from the heart. Large arteries branch into microscopic arteries called arterioles. Capillaries, the smallest and most numerous of the blood vessels, form the connection between the arteries and the venules and veins that return blood to the heart. The primary function of capillaries is the exchange of materials between the blood and tissue cells. By National Cancer Institute, National Institutes of Health (U.S.A.) Public Domain, https://commons.wikimedia.org/w/index.php?curid=45154160.

In fact, we have to distinguish two major types, depending on whether the vessel diameter is comparable to the size of red blood cells (RBCs) or not (see Figure 1). Human RBCs have the shape of a disk with a diameter of 7–8 μ m and a thickness of 2–38 μ m (slightly less in the middle, so that the volume is $\approx 908 \, \mu \text{m}^3$) and are quite flexible. The latter property is of fundamental importance because when the erythrocytes reach the very small vessels, the capillaries, where they release their O_2 charge in exchange for the CO_2 accumulated in the tissue, they must bend, as the vessel diameter can be almost half the cell diameter. If they fail to do so, this leads to a serious obstruction of blood circulation with various, even fatal, consequences. This is the case with Sickle Cell Disease, a disease caused by a defective hemoglobin structure. No model of fluid dynamics can describe the blood flow in the capillaries, as the composite structure of the blood becomes dramatically visible and the erythrocytes account for almost half of the blood volume (the normal value of hematocrit H, i.e., the percentage of erythrocytes by mass, in humans is 41–50% in men and 36–45% in women).

At this level, blood does not have to be examined as a heterogeneous fluid, but plasma and erythrocytes must be considered separately [28,72]. Apart from the extreme case of capillaries, the composite nature of blood also has remarkable consequences for flow in not so small but still small vessels such as venules and arterioles (see Figure 1), in the range of at least 6–7 times the diameter of erythrocytes up to half a millimeter. Strange phenomena have indeed been observed for a long time, but only recently have they received an explanation on a solid physical basis, which also allows us to better interpret their physiological significance. The first phenomenon we are concerned with

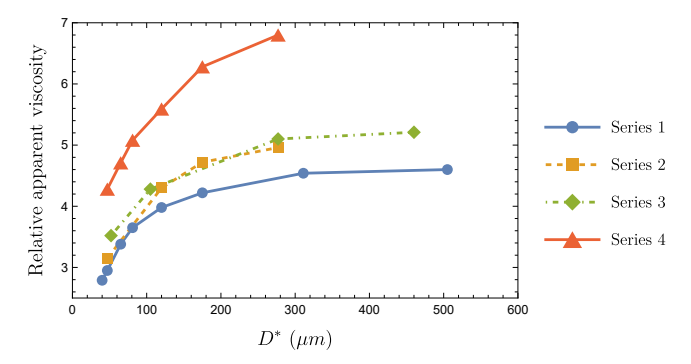


FIGURE 2. Original data from the Fåhræus–Lindqvist experiment [22]. The measured viscosity is relative to that of the plasma.

is the Fåhræus–Lindqvist (FL) effect. This occurs in blood vessels with a diameter in the range of 50–300 µm and is named after the two Swedish scientists Robin Fåhræus and Johann Torsten Lindqvist [22]. During their experiments with their own³ blood, they discovered an unexpected phenomenon: the *apparent*⁴ viscosity of the blood depends on the diameter of the tube if it is smaller than 300 µm. Even more surprising is that the apparent viscosity decreases with decreasing tube diameter; see Figure 2.

The same phenomenon was observed somewhat earlier by another team independently [58]. The problem of justifying the FL effect on a strictly fluid dynamic basis has long been an open issue [72]. Indeed, blood in tubes such as veins and arteries above a size of $\approx 300\,\mu m$ and at a relatively high shear rate ($\geq 100\,s^{-1}$) exhibits the characteristic Newtonian behavior of an incompressible fluid despite its composite (particulate) nature. On a smaller scale, however, this no longer applies, as inhomogeneity effects become very significant and must be taken into account. What physical mechanisms are responsible for such a counterintuitive phenomenon on a microscopic scale? This puzzling question has long remained unanswered.

Robert Haynes made an important contribution in this direction almost thirty years after Fåhræus and Lindqvist [46]. The main idea in Haynes' work is that the erythrocytes

⁽³⁾ See [22, p. 563].

⁽⁴⁾ This adjective when used jointly with viscosity typically refers, in rheology, to the measured viscosity of a fluid at a specific shear rate. If the fluid viscosity changes as the shear rate changes, this is a hallmark of non-Newtonian behavior. However, in the context of blood microcirculation, the influence of shear rate on blood viscosity is often much less significant than other factors, such as vessel diameter or hematocrit. These factors tend to dominate blood flow properties in microcirculation, so while blood exhibits non-Newtonian behavior in a broader sense, the apparent viscosity in this context is not primarily governed by shear rate as it would be for other classic non-Newtonian fluids (like polymer solutions or suspensions).

reorganize their movement to form a core-annular flow, with a large percentage of plasma remaining confined in the peripheral ring and a large percentage of erythrocytes in a central core. The physical reason for this is reminiscent of Jeffrey's [48] idea that the natural configuration of motion of a fluid suspension in a vessel is one in which dissipation caused by friction with the wall is minimized. Although Haynes' idea is suggestive and has been confirmed by recent observations [14, 39, 52], it has not been supported by rigorous evidence. Only recently have some new papers been published that aim to rigorously prove both Haynes' idea and the FL effect [26,43]. Moreover, the core-annular flow structure hypothesized by Haynes was recently shown to be stable in [34, 35]. The mathematical model in this work was then successfully tested with classical experiments. In addition to the focus on modeling, Ascolese et al. [3] also emphasized the role of the FL effect for life, to which we devote Sections 2.1, 2.2 and 2.3.

The second fascinating aspect of microcirculation that we will discuss below is the Fåhræus (F) effect, which was discovered by Robin Fåhræus [21] in 1929. Once again, we are dealing with a phenomenon that defies intuition. It would be reasonable to expect the hematocrit to remain the same regardless of vessel size. Instead, Fåhræus found that as the vessel diameter decreases, the hematocrit of the blood in the vessel also decreases. There is no doubt that Fåhræus was fully aware that what he discovered in 1931 together with Lindqvist was closely related to what he had discovered in 1929. The two effects must be directly related, but how can this be explained? From the point of view of physical intuition, the F effect is even more surprising than the FL effect.

Experiments reporting the F effect are fewer in number than those relating to the FL effect, partly due to the difficulty of limiting the errors associated with any measurement of hematocrit [4,5,14,36–38,40,49]. While the measurement of blood viscosity as a function of vessel diameter is essentially a measurement of volumetric flow rate followed by an application of Poiseuille's law, to measure hematocrit one must stop the flow, draw a blood sample in the capillary tube and then measure the percentage of solid mass (RBCs). This procedure is associated with large uncertainties. In Section 3.1, it is shown that the F-effect can also be modeled on a fluid dynamic basis [23]. It will not surprise us that the leading ideas and the arguments put forward to justify the FL effect are closely related.

As for the FL effect, one would like to know if there is a physiological reason that causes the blood flow to rearrange its cellular components according to the F effect. This question is addressed in Section 3.3, where, following [3,24], it is shown that the F-effect increases tissue perfusion.

The last part of this paper, Section 4, is devoted to vasomotion. This phenomenon consists of periodic radial oscillations of the vascular wall which are not related to the heartbeat. It occurs in arterioles and venules, both of which are surrounded by muscle

cells. It was first observed by the Scottish ophthalmologist Thomas Wharton Jones [50] in the venules that run along the bat wing membrane, whose structure is particularly well suited for the observations. There is a fundamental difference between vasomotion in venules and arterioles, as only the former are equipped with valves that convert the oscillations into a driving mechanism. The latter effect is very important, considering that in the venous system, the hydraulic pressure gradient of the blood is very low. For the historical and anatomical details, we refer to the book [29, Chapter 1.5], as well as to the paper [27]. In addition, we recall the paper [53], modeling the underlying physiological mechanism.

It must be emphasized that this phenomenon has considerable characteristics that severely impair blood flow. Typical values for the oscillation frequency are around 10 cpm (or 0.17 Hz), with an amplitude of 25% of the mean vessel diameter, but under exceptional conditions, a frequency of 25 cpm (0.42 Hz) and even 100% amplitude have been observed [47]. The oscillations are not symmetrical in the contraction phase (faster) and in the expansion phase (slower). For many years, there has been widespread agreement that vasomotion contributes effectively to the regulation of blood perfusion in the tissues [10, 17, 33, 47, 68, 69, 77].

The first mathematical model of vasomotion of venules based on the fundamental equations of fluid dynamics (Navier–Stokes equations and incompressibility condition) was presented in [25] as part of a more general study of peristaltically driven flows in vessels with an inlet and an outlet valve. A variant of the model that improves the fit to experimental data was presented in [9]. Vasomotion is in fact a limiting case of peristalsis, where the wavelength of peristalsis is much larger than the length of the channel, so that the wall profile is practically straight at all times.

In Section 4.1, we examine the case of the arterioles. An early attempt to model vasomotion in arterioles was presented in [60,61] by simply assuming a sinusoidal wall oscillation and averaging the blood outflow through the vessel over a certain period of time. The authors concluded that the effect of vasomotion is to increase outflow, but this contradicts the experimental results reported in [41,42]. In fact, the actual consequence of vasomotion is the opposite, as the vessel cross-sectional area is periodically reduced, a circumstance that has an unfavorable effect on the flow rate. The contradiction arises from the fact that in [61], the authors took the mean vessel radius as the reference value and not the one corresponding to the configuration in which the smooth muscle cells are at rest (unstretched) and the lumen is therefore the largest possible. So the legitimate question arises: if the vasomotion of arterioles is not beneficial for blood flow rate, what is it for? The answer came recently with the paper [23], in which it was shown that the oscillations with different frequencies of the vessels afferent to an arteriolar tree can periodically direct the blood flow to one sector rather than another due to the corresponding phase shift.

The mathematical model proposed in [23] confirms the experiments of Lapi et al. [56]. Indeed, capillary blood flow is modulated by changes in the diameter of the terminal arterioles, which facilitates the redistribution of blood flow according to the metabolic requirements of the tissue. In Section 4.2, we investigate vasomotion in combination with the FL effect. The latter indeed works in the opposite direction by increasing both discharge and energy dissipation, but the combination of the two phenomena ultimately proves to be beneficial. In Section 4.3, we compare the average hydraulic resistance provided by the mathematical model for vasomotion in arterioles with the experimental data from Gratton et al. [42]. Even if an uncertainty of 30% of the measured values is taken into account, the correction induced by the FL effect seems to satisfactorily fulfil the available data.

Finally, in Section 4.5, we discuss vasomotion in venules. This topic has been studied in several recent papers [9,18,25,27]. The situation is radically from arterioles, not only because of the presence of valves, but also because of the sharp reduction in the pressure gradient (blood pressure drops dramatically as the blood crosses the capillary network with high resistance) and because the longitudinal velocity of the blood is much smaller by one order of magnitude. In the absence of valves and at very low pressure gradients, vasomotion would make blood flow forward and backward in the vessel during a period. There is no backflow in venules because there are inlet and outlet valves. Therefore, Section 4.5 is largely dedicated to the presentation of the results of [25], where a mathematical model is developed to explain the experimental observations of Dongaonkar et al. [18] for vasomotion in a bat wing.

2. Modeling the Fähræus–Lindovist effect

If blood is considered a homogeneous Newtonian fluid, so that stress and shear rate are directly proportional due to a constant viscosity η^* (the temperature dependence plays no role here), equation (1.1) can be easily proven in the case of a cylindrical pipe and for a laminar flow. The equations of fluid motion (Navier–Stokes equation) can be solved explicitly for the axial velocity $u^*(r^*)$, which has a parabolic profile on the cross-section. Thus, computing the volumetric discharge through

(2.1)
$$Q^* = 2\pi \int_0^{R^*} r^* u^*(r^*) dr^*,$$

formula (1.1) is theoretically justified, and we can recover viscosity from a measure of discharge

(2.2)
$$\eta^* = \frac{\pi R^{*4}}{8L^*Q^*} \Delta P^*.$$

If blood were Newtonian, its viscosity should not depend on the tube radius. On the contrary, the experimental data by Fåhræus and Lindqvist, summarized in Figure 2, show that this is not true.

The measured viscosity is therefore referred to as "apparent" viscosity and is expressed as η_{app}^* , as it is not a property of the liquid but depends on the vessel radius. In particular, Figure 2 shows that the blood changes from a Newtonian behavior (constant viscosity) to a non-Newtonian behavior as soon as the vessel diameter falls below a critical threshold value (300 μ m).

To justify this peculiar behavior, we recall in Section 2.1 Haynes' so-called conjecture [46], which states that the erythrocytes leave the wall and migrate in an inner core of the vessel. We refer in particular to the recent article by Ascolese et al. [3], which highlights the actual physiological benefits of the FL effect. In Section 2.2, we then summarize the recent work of Guadagni and Farina [43], who have explained Haynes' conjecture as an input effect on a solid theoretical basis. Finally, according to [26], we show in Section 2.3 how the previous results can be combined to obtain a model for the apparent viscosity that fits the experimental data quite well.

2.1. Haynes' hypothesis and its consequences

There are several qualitative explanations for the non-Newtonian behavior of blood in small tubes. The most important one is related to the fact that blood is not a simple liquid, but an inhomogeneous suspension of different particles. Of all these particles, erythrocytes make up by far the largest proportion. In the sequel, we briefly present Haynes' hypothesis [46], which was the first to attempt to interpret the FL effect as the result of an "intelligent" reaction of the RBCs to the narrowing of the vessel diameter. The erythrocytes in vessels with a diameter less than about 300 µm tend to migrate to the central part of the vessel, a phenomenon that only recently has been explained on a rigorous physical basis [43]. Accordingly, a less viscous layer forms near the walls, usually referred to as the "marginal zone", whose viscosity, denoted by η_a^* , is close to that of the plasma, since the amount of RBCs in it is very small. According to Haynes, the physiological advantage for the migration of erythrocytes to the center of the tube is the reduction of the heart workload. Since the viscosity of the marginal layer is from 4 to 5 times lower than that of the core, the wall stress is drastically reduced and so the migration of the RBCs toward the center of the tube seems to reduce the heart effort⁵. However, we will show that this heuristic explanation is misleading.

(5) Haynes' central idea is somewhat reminiscent of the theory of Jeffery [48], who put forward the heuristic hypothesis that particles tend to adopt the motion that corresponds to the least energy dissipation.

A recent reference concerning the experimental evidence of the *cell poor layer* is Stergiou et al. [74], who have been able to effectively provide some measure. An updated reference concerning the measurement of the cell poor layer can be found in the PhD thesis by Gliah [39] (see also [52]).

Following [46] (we refer the readers also to [3] for more details), we consider the blood as an inhomogeneous incompressible linear viscous fluid, whose viscosity depends on the hematocrit H, i.e., $\eta^* = \eta^*(H)$. Denoting by u^* and P^* the fluid velocity and pressure, the continuity and momentum balance equations are

(2.3)
$$\frac{\partial^* H}{\partial t^*} + \boldsymbol{u}^* \cdot \nabla^* H = 0,$$

$$\nabla^* \cdot \boldsymbol{u}^* = 0,$$

$$\varrho^* \left(\frac{\partial^* \boldsymbol{u}^*}{\partial t^*} + (\nabla^* \boldsymbol{u}^*) \boldsymbol{u}^* \right) = -\nabla^* P^* + \nabla^* \cdot \mathbb{T}^*,$$

where ϱ^* is the blood density, and

$$\mathbb{T}^* = 2\eta^*(H)\mathbb{D}^*$$

is the deviatoric part of the Cauchy stress with $\mathbb{D}^* = (1/2)(\nabla^* u^* + \nabla^* u^{*T})$. Concerning $\eta^*(H)$, the current literature offers several empirical laws (see, for example, [8, 12, 15, 45, 54, 63]), in the absence of a general theory to relate η to H, where η is the blood viscosity relative to plasma; that is,

$$\eta = \frac{\eta^*}{\eta_n^*},$$

with η_p^* plasma viscosity. All the quoted empirical formulas can be written as

(2.6)
$$\eta(H) = \frac{1}{f(H)},$$

where $f:[0,H_{\max})\to (0,1]$, with $H_{\max}<1$, $f'(H)\leq 0$, and f(0)=1 (see Table 1). We now consider a cylindrical tube whose diameter is $D^*=2R^*$ and whose length is L^* . Denoting by r^* the radial coordinate and assuming

$$u^* = u^*(r^*) e_x, \quad H = H(r^*), \quad \Delta P^* = P^*(0) - P^*(L^*),$$

where e_x is the unit vector parallel to the cylinder axis, we have

(2.7)
$$u^*(r^*) = \frac{\Delta P^*}{2L^*} \int_{r^*}^{R^*} \frac{\zeta^*}{\eta^*(H(\zeta^*))} d\zeta^*$$

if no-slip boundary conditions are considered. Here, we are neglecting the short transient

| f(H) | Reference |
|---|-----------|
| $f_{\text{ChKu}}(H) = 1 - 0.07H \exp \left[2.49H + \frac{1107}{T} \exp(-1.69H) \right] $ (<i>T</i> in Kelvin) | [12] |
| $f_{\mathrm{Hat}}(H) = 1 - H^{\frac{1}{3}}$ | [45] |
| $f_{\text{Co}}(H) = (1 - H)^{2.5}$ | [15] |
| $f_{\text{B\&W}}(H) = 1 - H$ | [8] |
| $f_{\text{Nu}}(H) = \frac{0.75 - H}{0.75}$ (with $H < 0.75$) | [63] |
| $f_{\text{KrDo}}(H) = \left(1 - \frac{H}{0.67}\right)^{1.82} \text{ (with } H < 0.67)$ | [54] |

Table 1. Most used empirical formulas to estimate blood viscosity.

phase leading to the core-annular structure. Following Haynes' conjecture, $H(r^*)$ and, consequently, viscosity are step-wise functions

$$(2.8) \quad H(r^*) = \begin{cases} H_c, & 0 \le r^* \le s^*, \\ H_a, & s^* < r^* \le R^*, \end{cases} \quad \eta^*(H) = \begin{cases} \eta_c^* = \eta^*(H_c), & 0 \le r^* \le s^*, \\ \eta_a^* = \eta^*(H_a), & s^* < r^* \le R^*, \end{cases}$$

 s^* being the radius of the inner core, and where subscripts "c" and "a" stay for "core" and "annulus", respectively. Clearly, (2.8) is a simplifying assumption aimed to obtain explicit formulas, for example, for blood velocity (as (2.9)). However, (2.7) has a wider validity.

The fact that the outer layer is not completely devoid of RBCs has been suggested by several authors [20, 52]. That amount of RBCs present in the marginal layer has some variability although we expect H_a to be significantly smaller than H_c .

Of course, s^* is not arbitrary since the flow of incoming erythrocytes must be preserved along the x-axis. The continuity of velocity and shear stress at the interface s^* allows obtaining (see [3] for details) the velocity profile in the whole tube

(2.9)
$$u^*(r^*) = \begin{cases} \frac{\Delta P^*}{4L^*} \left(\frac{s^{*2} - r^{*2}}{\eta_c^*} + \frac{R^{*2} - s^{*2}}{\eta_a^*} \right), & 0 \le r^* \le s^* \\ \frac{\Delta P^*}{4L^*} \frac{R^{*2} - r^{*2}}{\eta_a^*}, & s^* < r^* \le R^*, \end{cases}$$

and, setting

$$(2.10) s = \frac{s^*}{R^*} \in (0, 1],$$

the central core discharge

(2.11)
$$Q_c^* = \frac{\pi \Delta P^*}{8L^*} \left(\frac{s^{*4}}{\eta_c^*} + \frac{2(R^{*2} - s^{*2})s^{*2}}{\eta_a^*} \right)$$
$$= \frac{\pi \Delta P^*}{8L^*} \frac{R^{*4}}{\eta_a^*} \left[\frac{\eta_a^*}{\eta_c^*} s^4 + 2s^2 (1 - s^2) \right] \quad \text{(core)},$$

the outer annulus discharge

(2.12)
$$Q_a^* = \frac{\pi \Delta P^*}{8L^*} \frac{(R^{*2} - s^{*2})^2}{\eta_a^*} = \frac{\pi \Delta P^*}{8L^*} \frac{R^{*4}}{\eta_a^*} (1 - s^2)^2 \quad \text{(outer layer)}$$

and the total discharge

$$(2.13) Q^* = \frac{\pi \Delta P^*}{8L^*} \left(\frac{s^{*4}}{\eta_c^*} + \frac{R^{*4} - s^{*4}}{\eta_a^*} \right) = \frac{\pi \Delta P^*}{8L^*} \frac{R^{*4}}{\eta_a^*} \left[\frac{\eta_a^*}{\eta_c^*} s^4 + (1 - s^4) \right].$$

The model that allows the determination of *s* as a function of both the fluid rheology and the geometric characteristics of the RBCs is discussed in Section 2.2.

The total power dissipation by the viscous friction along the tube is

(2.14)
$$W^* = 2\pi \int_0^{L^*} \int_0^{R^*} \eta^* (H(r^*)) \left(\frac{du^*}{dr^*}\right)^2 r^* dr^* dx^*$$
$$= \frac{\pi}{8} \frac{\Delta P^{*2}}{L} \frac{R^{*4}}{\eta_a^*} \left[\frac{\eta_a^*}{\eta_c^*} s^4 + (1 - s^4)\right].$$

Thus, by using (2.13), it follows that

$$(2.15) W^* = \Delta P^* Q^*,$$

as expected. In order to evaluate the effect of the marginal layer on both the volumetric flow rate and the total dissipation, let us work on the expression (2.13) introducing the dependence of viscosity on the hematocrit.

Assuming, for the sake of simplicity, that $H_a = 0$ (actually very minor changes allow the case $H_a > 0$ to be treated as we shall show in Section 3.3) so that $\eta_a^* = \eta_p^*$ and exploiting (2.6), formula (2.13) rewrites as

(2.16)
$$Q^* = \frac{\pi \Delta P^*}{8L^*} \frac{R^4}{\eta_p^*} \left[f(H_c) s^4 + (1 - s^4) \right]$$
$$= \frac{\pi \Delta P^*}{8L^*} R^4 \underbrace{\left(\frac{f(H_B)}{\eta_B^*} \right)}_{1/\eta_B^*} \frac{f(H_c) s^4 + (1 - s^4)}{f(H_B)},$$

where η_B^* and H_B are the viscosity and hematocrit of the blood entering the vessel. The key point of the theory developed by Ascolese et al. in [3] is that $f(H_c)$ can be expressed via s and H_B . Indeed, imposing the RBCs, mass conservation (and assuming, as already mentioned, $H_a = 0$), we have

$$(2.17) Q^* H_B = Q_c^* H_c,$$

which, recalling (2.11), (2.13) and (2.6), yields

(2.18)
$$\frac{H_c}{H_B} = 1 + \frac{(1 - s^2)^2}{s^2 [2 - 2s^2 + s^2 f(H_c)]}.$$

It is worth noticing that there exists a lower limit for s, say s_{\min} , corresponding to $H_{c,\max}$, the maximum allowable for H_c . The latter cannot be realistically taken equal to 1 since some plasma remains, anyway, trapped within the RBCs core. However, we can, practically, identify the maximum of H_c with that for which f=0. Doing so, we find

(2.19)
$$s_{\min} = \left(\frac{H_{\text{c,max}}}{2H_R} - 1\right)^{-1/2}.$$

We note the physical coherence of (2.18). Namely, if s=1, i.e., the marginal zone disappears, then $H_c=H_B$. Conversely, with $H_c=H_B$, we necessarily have s=1 due to the fact that f<1. Formula (2.18) establishes a link between s and H_c which, by applying the implicit function theorem, allows expressing H_c as a function of s and H_B , depending of course on the selected f; namely,

$$(2.20) H_c = \chi_f(s, H_B).$$

Plugging (2.20) in (2.16) and normalizing Q^* with $Q_B^* = \frac{\pi \Delta P^* R^4}{8L^* \eta_B^*}$, we obtain

(2.21)
$$Q = \frac{Q^*}{Q_B^*} = \Psi(s, H_B, f),$$
 with $\Psi(s, H_B, f) = \frac{f[\chi_f(s, H_B)]s^4 + (1 - s^4)}{f(H_B)}.$

Proceeding similarly for W^* , we have

(2.22)
$$W = \frac{W^*}{W_B^*} = \Psi(s, H_B, f),$$

where $W_B^* = \frac{\pi(\Delta P^*)^2 R^{*4}}{8L^*\eta_B^*}$. Figures 3, 4 and 5 show the function Ψ for all functions f considered in Table 1.

We note that Ψ is a strictly decreasing function of s. In particular, for all f considered, $\frac{\partial \Psi}{\partial s} < 0$ for $s \in (s_{\min}, 1)$ and $\Psi \to 1$ as $s \to 1$. Therefore, formula (2.22) states that W increases with decreasing s; i.e., the larger the marginal layer, the greater the dissipation. At the same time, Q, which is given by (2.21), also increases, which in physiological terms means an increase of the perfusion rate towards the peripheral tissue. This conclusion illustrates more than others the crucial role of the FL effect in physiology, which is actually to improve the organs, blood perfusion.

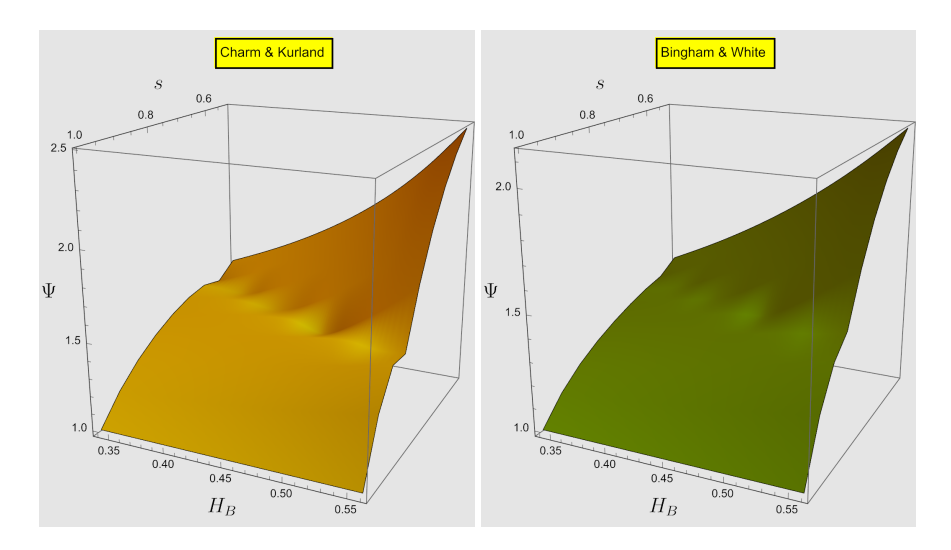


FIGURE 3. The function Ψ in two cases (Charm & Kurland in the left panel, Bingham & White in the right panel).

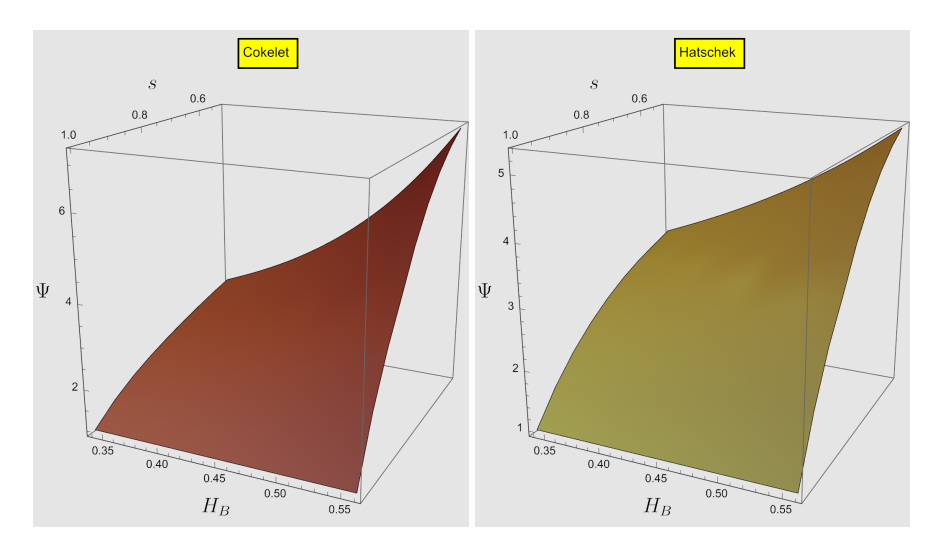


FIGURE 4. The function Ψ in two cases (Cokelet in the left panel, Hatschek in the right panel).

2.2. The marginal layer explained as an entrance effect

In this section, based on the fundamental laws of fluid mechanics, we show that Haynes' conjecture has a physical explanation and that it is the correct basis for a rigorous fluid dynamic interpretation of the FL effect. We have already illustrated that the marginal region and the inner core are separated by an interface whose radius is denoted by s^*

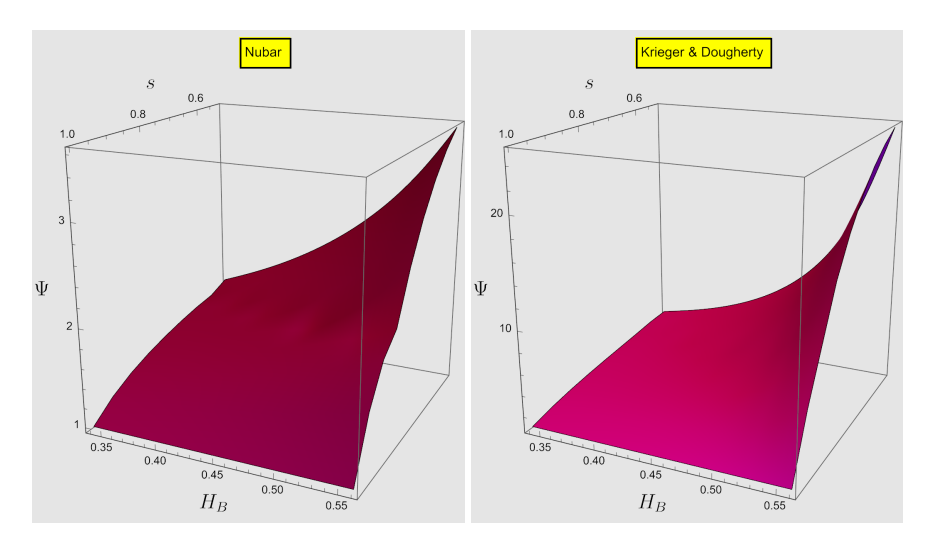


FIGURE 5. The function Ψ in two cases (Nubar in the left panel, Krieger & Dougherty in the right panel).

and is a function of the longitudinal coordinate x^* along the vessel. Indeed, our analysis relies on the recent results of Guadagni and Farina [43], which show that the motion of the particles towards the channel axis can be explained as an entrance effect (i.e., in terms of the radial velocity generated when the cells enter the vessel) and that, actually, the flow soon reaches a core-annulus structure. Particle migration towards the center of blood vessels has also been studied by other researchers. In 1948, Vand [75] observed that the measured viscosity of a suspension of rigid spheres is affected by the presence of walls, as if there were a layer of thickness δ along each wall, with the viscosity equal to that of the pure liquid. In 2001, Sharan and Popel [73] proposed a two-phase model for blood flow in narrow tubes, solving a consistent system of nonlinear equations numerically to estimate the thickness of the cell-free layer. However, their estimate was partly based on empirical formulas.

In contrast, in 2020, the analysis by Guadagni and Farina [43] provided an explicit and rigorous formula that directly relates the initial thickness of the layer to its asymptotic value. This formula has proven to be crucial for our approach to modeling both the FL effect and the F effect.

A key step is to define the marginal layer thickness at the very entrance of the vessel, i.e. the difference between the vessel radius R^* and $s^*|_{x^*=0} = s_0^*$. In the literature, this thickness is attributed to the so-called "size exclusion effect" [20,70,72]. Concerning RBCs, which have a discoid shape, such a size should not exceed the discoid maximal thickness ($\approx 2-3 \,\mu\text{m}$) because RBCs enter the vessel in a configuration which offers the least surface in the flow direction. Thus, denoting by a^* the size of this

layer, i.e., $a^* = R^* - s_0^*$, it is reasonable to guess that a^* is going to depend on the geometrical properties of the RBCs; namely, $a^* \approx 1-2 \, \mu m$. In [43], the authors show that, downstream, both the core radius and the velocity field stabilize to their asymptotic values, i.e., s_{∞}^* and $u^*(r^*)e_x$, where $u^*(r^*)$ is given by (2.9).

The main point of the model is that there is a relationship between s_{∞}^* and s_0^* since the core surface is a material surface. If u_{in}^* is the axial entry velocity (uniform on the cross-section), we can write

(2.23)
$$\pi u_{\text{in}}^* s_0^{*^2} = 2\pi \int_0^{s_\infty^*} u^*(r^*) r^* dr^*.$$

Now, recalling (2.10) and setting

$$(2.24) s_0 = \frac{s_0^*}{R^*} = 1 - \frac{a^*}{R^*} = 1 - \frac{2a^*}{D^*}, \quad s_\infty = \frac{s_\infty^*}{R^*},$$

equation (2.23) can be rewritten as⁶

$$(2.25) s_0^2 = \frac{1}{s_\infty^4 \left(\frac{1}{\eta_c^*} - \frac{1}{\eta_a^*}\right) + \frac{1}{\eta_a^*}} \left[s_0^4 \left(\frac{1}{\eta_c^*} - \frac{2}{\eta_a^*}\right) + \frac{2s_\infty^2}{\eta_a^*} \right],$$

which is a fourth-order algebraic equation in the unknown s_{∞} , with only one physically significant solution, i.e. $s_{\infty} \in (0, 1)$,

(2.26)
$$s_{\infty} = \frac{s_0}{\sqrt{1 + \sqrt{(1 - s_0^2) \left[1 - s_0^2 \left(1 - \frac{\eta_a^*}{\eta_c^*}\right)\right]}}.$$

2.3. The Fåhræus–Lindqvist effect theoretically justified

Now, as in [26], we assume

(2.27)
$$\eta_a^* = \eta_p^* + \alpha (\eta_c^* - \eta_p^*),$$

and $0 \le \alpha \le \mathcal{O}(10^{-1})$ is a fitting parameter. Physically, this means that we do not consider the marginal layer to be completely free of RBCs. A reasonable explanation could be that the "marginal exclusion effect" cannot be precisely specified (as would be the case if the RBCs were rigid spheres) and should rather be understood as a statistical concept (see e.g. Ethier and Simmons [20]). Therefore, it is acceptable to assume that a small hematocrit is present in the marginal layer and that this value may show some variability (Kim et al. [52] also refer to the outer layer as the "cell-poor" region).

Recalling (2.2), which essentially defines η_{app}^* , we get

(2.28)
$$\eta_{\text{app}}^* = \frac{\eta_a^*}{1 + s_\infty^4 \left(\frac{\eta_a^*}{\eta_c^*} - 1\right)} = \frac{\eta_p^* + \alpha(\eta_c^* - \eta_p^*)}{1 + s_\infty^4 \left(\frac{\eta_p^* + \alpha(\eta_c^* - \eta_p^*)}{\eta_c^*} - 1\right)}.$$

Introducing now the relative apparent viscosity, $\eta_{\rm app} = \eta_{\rm app}^*/\eta_p^*$, and the relative core viscosity, $\eta_c = \eta_c^*/\eta_p^*$, we have

(2.29)
$$\eta_{\text{app}} = \frac{1 + \alpha(\eta_c - 1)}{1 + s_{\infty}^4 \left(\frac{1 + \alpha(\eta_c - 1)}{n_c} - 1\right)},$$

with s_{∞} given by (2.26), which, exploiting (2.27), we rewrite as

(2.30)
$$s_{\infty} = \frac{s_0}{\sqrt{1 + \sqrt{(1 - s_0^2) \left[1 - s_0^2 \left(1 - \frac{1 + \alpha(\eta_c - 1)}{\eta_c}\right)\right]}}.$$

Formula (2.29) establishes an explicit link between the apparent viscosity (relative to the plasma) and the vessel diameter, which is included in the expression via s_0 . In particular, it should be noted that $s_0 \to 1$ for large diameters and that $\eta_{\rm app}$ becomes that of the core, which in reality occupies the entire vessel and is therefore the viscosity of the in-flowing blood. The influence of the tube radius on the apparent viscosity becomes "important" when $2a^*/D^*$ is no longer negligible. We have thus obtained a theoretical justification for the FL effect, i.e., for the fact that the apparent viscosity of the blood depends on the diameter of the vessel in which it flows.

However, the model can only be considered satisfactory if it is able to reproduce the experimental data with reasonable values of the fitting parameters, which are α and a^* , which vary in a narrow range. The model has therefore been tested versus the experimental data by Fåhræus and Lindqvist [22], versus those by Kümin [55] and Zilow and Linderkamp [79] and versus the two well-known empirical formulas proposed by Pries [64],

(2.31)
$$\eta_{\text{app}}^{(P)}(D,H) = 1 + \left(\eta_{0.45}^{(P)}(D) - 1\right) \frac{(1-H)^{c(D)} - 1}{(1-0.45)^{c(D)} - 1},$$

where

(2.32)
$$\eta_{0.45}^{(P)}(D) = 220 \exp(-1.3 D) + 3.2 - 2.44 \exp(-0.06 D^{0.645}),$$

and

$$(2.33) c(D) = (0.8 + \exp(-0.075 D)) \left(\frac{1}{1 + 10^{-11} D^{12}} - 1\right) + \frac{1}{1 + 10^{-11} D^{12}},$$

and Secomb [72]

(2.34)
$$\eta_{\text{app}}^{(S)}(D, H) = \frac{d^2 \left(\frac{D^2 \left(\eta_{0.45}^{(S)}(D) - 1\right) \left((1 - H)^{c(D)} - 1\right)}{(D - 1.1)^2 (0.55^{c(D)} - 1)} + 1\right)}{(D - 1.1)^2}$$

where

(2.35)
$$\eta_{0.45}^{(S)}(D) = 3.2 - 2.44 \exp(-0.06 D^{0.645}) + 6 \exp(-0.085 D).$$

In all these relations, D denotes the dimensionless tube diameter, i.e. $D = D^*/D_{\rm ref}^*$, with $D_{\rm ref}^* = 1 \, \mu \rm m$ in our notation. These formulas are both based on the best-fitting procedure using several sets of data collected in the last seventy years. The comparison of our mathematical model [26] versus both data and the empirical formulas is shown in Figures 6, 7 and 8.

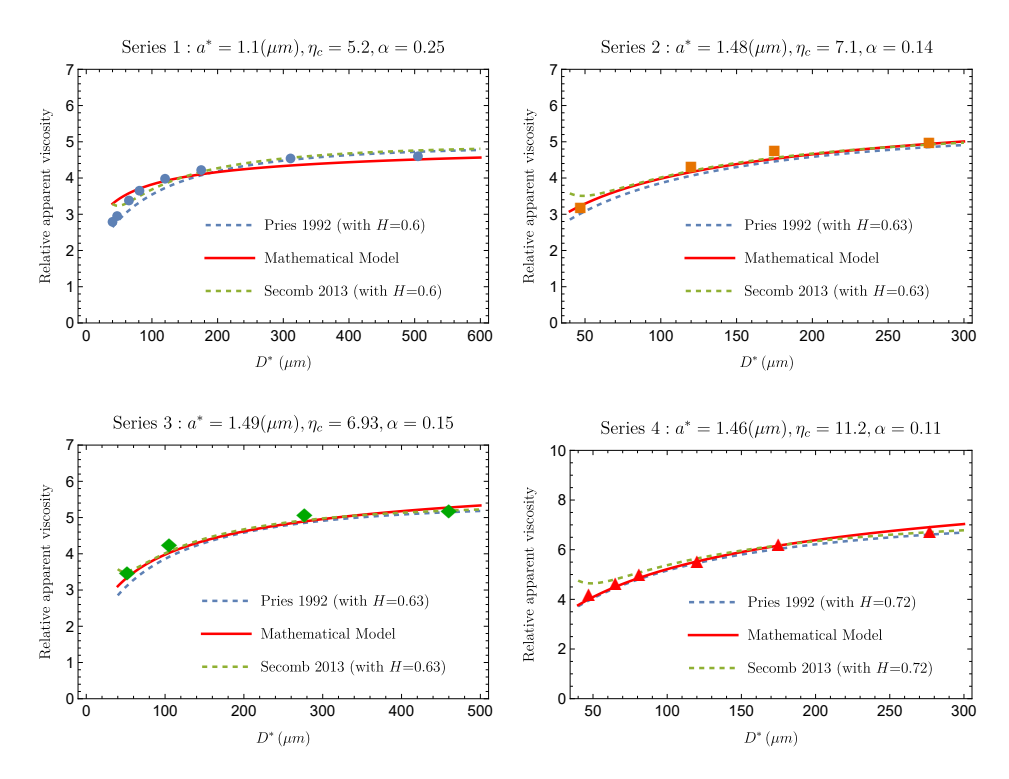


FIGURE 6. Comparison between the experimental series 1, 2, 3 and 4 reported in tables at p. 565 of Fåhræus and Lindqvist [22] (dots) and the theoretical model (see [26]) (2.29)–(2.30) (solid curve). The fitting via the empirical formulas (2.31) by Pries and (2.34) by Secomb is also shown (dashed curves). On the top of each plot, there are the values of a^* , α , η_c and the hematocrit H used in formulas (2.31)–(2.35) to fit the Fåhræus and Lindqvist data.

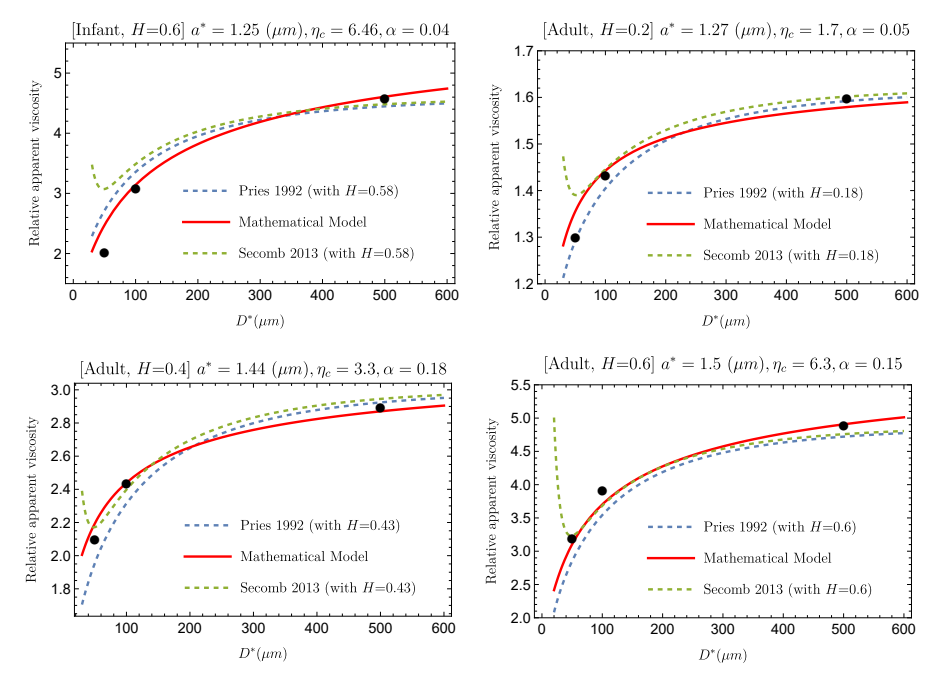


FIGURE 7. Comparison between our mathematical model (solid curve) (see [26]) and data by Zilow and Linderkamp [79] (dots). These authors considered both adult and infant blood samples at different values of the hematocrit. The empirical fitting via the empirical formulas (2.31) by Pries and (2.34) by Secomb is also shown (dashed curves).

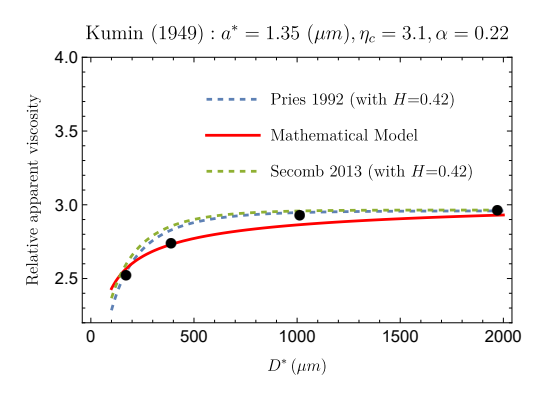


FIGURE 8. Comparison between our model (see [26]) and the experimental data by Kümin [55] (dots). Data are extracted from Figure 2, at p. 1195 of [46]. The empirical fitting via the empirical formulas (2.31) by Pries and (2.34) by Secomb is also shown (dashed curves).

3. The Fåhræus effect

Fåhræus' experiment considered a set of capillary tubes with decreasing diameter from $1,100 \,\mu m$ to $50 \,\mu m$. The hematocrit of the feeding reservoir was fixed at 40.5%.

| Tube diameter (mm) | Tube hematocrit H_T (%) | Plasma $(1 - H_T)$ | Rel. hematocrit H_R |
|--------------------|---------------------------|--------------------|-----------------------|
| 1.100 | 40.5 | 59.5 | 1 |
| 0.750 | 40.1 | 59.9 | 0.99 |
| 0.450 | 39.8 | 60.2 | 0.983 |
| 0.250 | 39.2 | 60.8 | 0.968 |
| 0.095 | 33.6 | 66.4 | 0.829 |
| 0.050 | 28.0 | 72.0 | 0.691 |

Table 2. Fåhræus' original data. The hematocrit in the reservoir is $H_F = 40.5\%$. The tube relative hematocrit, i.e. $H_R = H_T/H_F$, results by dividing data in the second column by H_F . The experiments show that H_R is rapidly (nonlinearly) decreasing by reducing the tube diameter.

By centrifuging the outlet blood, he measured an increase in the plasma content corresponding to a decreasing RBCs percentage as the tube diameter decreased, thus showing a decrease in the relative tube hematocrit (see Table 2).

Is there any physiological justification for the F effect? In Section 2.1, we showed that the FL effect helps the tissue perfusion (see Ascolese et al. [3]) increasing the blood flow rate. In the case of the F effect, things are not so clear. Indeed, the flow rates of both the fluid and cell components of blood are to be preserved along the whole blood loop through the body. Because of this fact, we may argue that the hematocrit reduction observed in the F effect is made possible by the simultaneous occurrence of the FL effect, which intervenes modifying the way the two species are carried along the flow, facilitating RBCs transport. We can even conjecture that precisely this puzzling question posed by the F effect pushed Fåhræus himself to further investigate the blood flow properties in smaller vessels, thus discovering the FL effect.

As pointed out by Barbee [5], one delicate point is the way the hematocrit is measured. Indeed, the measure of the blood viscosity as a function of the vessel diameter (the FL effect) is, essentially, a measure of the volumetric flow rate followed by an application of the Poiseuille law. On the other hand, for measuring the hematocrit one needs to stop the flow, take a blood sample in the capillary tube and then measure the solid mass (RBCs) percentage. This procedure induces a great uncertainty in the measure itself, which is one of the reasons for which there have been very few replicas of Fåhræus' experiment for the last 95 years, Barbee's PhD thesis being one of the few. Among these contributions, we mention [14,49].

Figure 9 (which reproduces Figure 2 of [6]) shows the *relative hematocrit*, i.e. the ratio H_T/H_F , as a function of both the reservoir hematocrit H_F and the tube diameter. It is quite evident that, for a given diameter, the function H_T/H_F is essentially linear in H_F and that its derivative increases by decreasing the tube diameter (see Figure 9). The latter effect also appears more pronounced for diameters below 100 μ m.

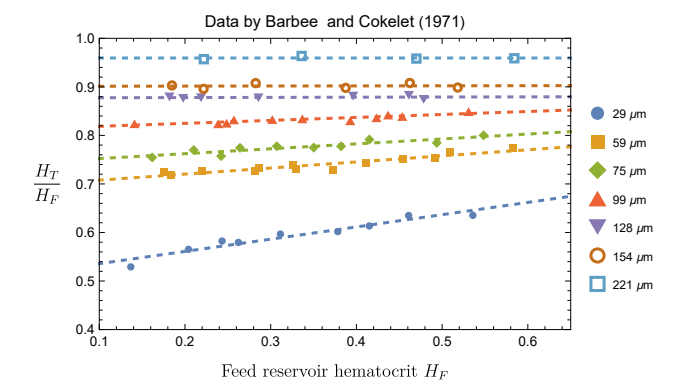


FIGURE 9. The relative tube hematocrit $H_R = H_T/H_F$ as a function of feed hematocrit H_F for various vessel diameters using human blood, according to Figure 2 in Barbee and Cokelet [6]. Dashed lines are linear fits.

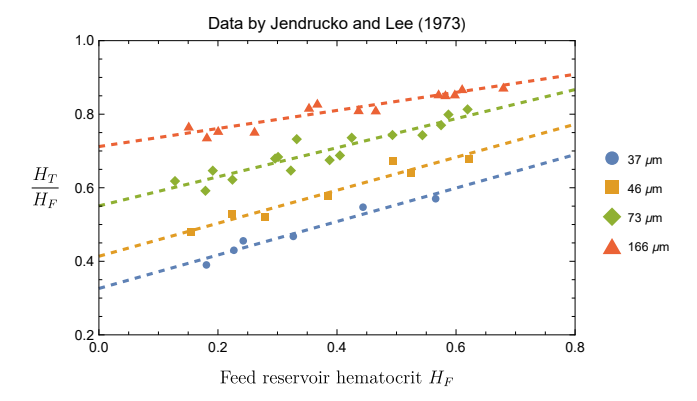


FIGURE 10. The relative tube hematocrit H_T/H_F as a function of feed hematocrit H_F for various vessel diameters, according to Figure A2 in Jendrucko and Lee [49]. In this case, cat blood was used. Dashed lines are linear fits.

Fåhræus' experiment uses human blood. Jendrucko and Lee [49] considered also the case of cat's blood (see Figure 10). This experiment is interesting because the cat's erythrocyte is smaller than the human one, about 6 μ m in the largest diameter of the former against 7.5–8 μ m in the latter. It is interesting to note that Jendrucko and Lee made their experiment for a specific diameter at a number of different flow rates. The results indicated that the flow rate has no measurable effect on the correlation between H_R and H_F , confirming a similar conclusion of Barbee and Cokelet.

All experiments available so far suggest for $H_R = H_T/H_F$ a linear relationship with H_F of the following type:

(3.1)
$$H_R = \mathfrak{F}(H_F, D^*) = A(D^*)H_F + B(D^*),$$

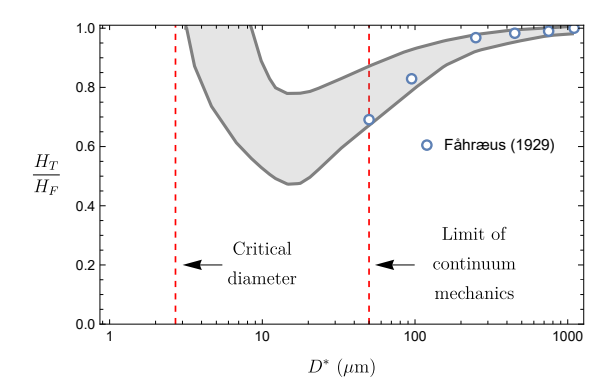


FIGURE 11. The relative tube hematocrit $H_R = H_T/H_F$ as a function of the tube diameter D^* : the shaded region includes all the data available from the original Fåhræus experiment to 1980, according to [36, Figure 4] and [40, Figure 1 (A)]. For a given D^* , the difference between the upper and lower curves provides the amplitude of the error bar. The critical diameter ($\approx 2.7 \, \mu m$) is that of the smallest cylindrical vessel through which a human red cell can flow. The limit of applicability of the continuum hypothesis is also indicated.

with

(3.2)
$$\frac{\partial \mathfrak{F}}{\partial H_F} = A(D^*) \ge 0, \quad \frac{\partial \mathfrak{F}}{\partial D^*} \ge 0,$$

at least as long as the dimensional diameter D^* remains in a finite interval from (approximately) 30 up to 220 μ m.

It must be emphasized that other researchers have investigated the F effect and that there is great uncertainty about the collected data, which increases significantly as the tube diameter decreases [36–38] (see Figure 11). Looking at the difference between the upper curve and the lower one in Figure 11, it turns out that for diameters in the interval (50,200) μ m, the measurement error decreases from $\approx 20\%$ to $\approx 5\%$, and decreases from this last value to 1% in the remaining part of the interval. Therefore, any mathematical model aimed at reproducing the F effect must take this uncertainty into account. For example, the data of Table 2 should be – more correctly – presented as in Figure 12, that is, including the error bands.

3.1. Modeling the Fåhræus effect

Here, we use the same geometry, symbols and scaling for the main physical quantities and the same model for the governing motion equations as in Section 2. In particular, we recall that all starred quantities are meant to be dimensional. Indeed, the basic machinery is the same as that used to develop our model for the FL effect, but now, in addition, the role of the hematocrit is carefully considered. We recall, once again, that

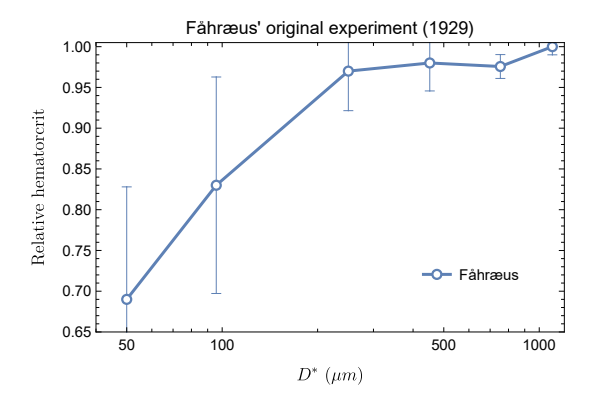


FIGURE 12. Graphical representation of Fåhræus' original data, emphasizing the size of possible errors when measuring H_R at rather small vessel diameter.

since we are using the continuum hypothesis, our analysis must necessarily exclude the case of too-small diameters. In particular, we must exclude both the case of 29 μ m in Figure 9 and the cases 37, 46 μ m in Figure 10.

Concerning the deviatoric part of the Cauchy stress tensor, we still assume (2.4), though, strictly speaking, this assumption is not correct in principle. Indeed, the independence of η^* on the shear rate is reasonable only if the shear rate is sufficiently large (say, $\geq 300 \, \mathrm{s}^{-1}$) [29, 72], which is not the case for a capillary flow. So, how can we justify our choice? Indeed, we will recognize a posteriori that, even ignoring the dependence of η^* on $|\mathbb{D}^*| = \sqrt{2 \, \mathrm{tr}(\mathbb{D}^*)^2}$, the model succeeds, anyway, in fully explaining the F effect.

Going into details, with $r^* = s^*(x^*)$ being the inner core material boundary, we rewrite (2.23) as

(3.3)
$$Q^* \left(\frac{s_0^*}{R^*}\right)^2 = 2\pi \int_0^{s_\infty^*} u^*(r^*) r^* dr^*,$$

where Q^* is the blood discharge. We recall that, in writing (3.3), we have implicitly assumed that the flow is uniform at the inlet cross-section, namely, $Q^* = \pi R^{*2} u_{\text{in}}^*$, with u_{in}^* inlet mean velocity appearing in (2.23).

Then, we recall that the hematocrit and viscosity radial profiles are step-wise functions given by (2.8).

In Section 2, we have seen that, using the assumption (2.8), the asymptotic dimensional velocity [3, 13] is given by (2.9), which can be rewritten in dimensionless form (see [26] for more details)

(3.4)
$$u(r) = \frac{2}{\frac{s_{\infty}^4}{\eta_c} + \frac{1 - s_{\infty}^4}{\eta_a}} \times \begin{cases} \frac{s_{\infty}^2 - r^2}{\eta_c} + \frac{1 - s_{\infty}^2}{\eta_a}, & 0 \le r \le s_{\infty}, \\ \frac{1 - r^2}{\eta_a}, & s_{\infty} \le r \le 1, \end{cases}$$

where, as in Section 2, $\eta_a = \eta_a^*/\eta_p^*$ and $\eta_c = \eta_c^*/\eta_p^*$, s_o and s_∞ are defined in (2.24) and where s_o and s_∞ are linked by (2.26).

The issue of the tube relative hematocrit as a function of the feeding hematocrit and the tube diameter was first considered by Barbee and Cokelet [6] continuing the deep analysis developed in Barbee's PhD thesis [5]. As already said, the hematocrit of the blood in the capillary tube is determined by stopping the flow and then by pouring the trapped suspension into a specific device for the hematocrit measurement [6]. Hence, H_T is a volume averaged hematocrit (see also [70, pp. 152–153])

(3.5)
$$H_T = \frac{\int_0^{L^*} \int_0^{R^*} \int_0^{2\pi} Hr^* dr^* d\vartheta dx^*}{\pi R^{*2} L^*}.$$

Because of (2.8), equation (3.5) implies

(3.6)
$$\frac{H_T}{H_E} = \frac{H_c}{H_E} s_{\infty}^2 + \frac{H_a}{H_E} (1 - s_{\infty}^2).$$

We need now to estimate H_c in terms of H_F . Leaving aside the complex phenomena taking place at the tube entrance, we proceed as in Section 2.2, assuming a discontinuity across x=0 in the RBCs radial distribution, which is uniform for $x=0^-$ (side of the entrance facing the reservoir) and stepwise for $x=0^+$ (side of the entrance facing the tube). Thus, imposing the RBCs mass conservation across x=0, we have

(3.7)
$$\pi R^{*2} u_{\text{in}}^* H_F = \pi s_0^{*2} u_{\text{in}}^* H_c + \pi (R^{*2} - s_0^{*2}) u_{\text{in}}^* H_a.$$

Concerning H_a , we follow the approach pursued in (2.27) and, using a similar notation, we set $H_a = \alpha H_c$, typically $\alpha \leq \mathcal{O}(10^{-1})$. The value $\alpha = 0$ corresponds to an outer layer free from RBCs. Then, from (3.7), we get

(3.8)
$$\frac{H_c}{H_F} = \frac{1}{s_0^2 + \alpha(1 - s_0^2)},$$

so that

(3.9)
$$H_R = \frac{H_T}{H_F} = \frac{s_\infty^2 + \alpha (1 - s_\infty^2)}{s_0^2 + \alpha (1 - s_0^2)}.$$

Recalling now (2.8), we have

(3.10)
$$\eta = \begin{cases} \eta_a = \eta(\alpha H_c), & s \le r \le 1, \\ \eta_c = \eta(H_c), & 0 \le r \le s, \end{cases}$$

and, exploiting (2.26), we deduce that

(3.11)
$$s_{\infty}^{2} = \frac{s_{0}^{2}}{1 + \sqrt{(1 - s_{0}^{2}) \left[1 - s_{0}^{2} \left(1 - \frac{\eta(\alpha H_{c})}{\eta(H_{c})}\right)\right]}},$$

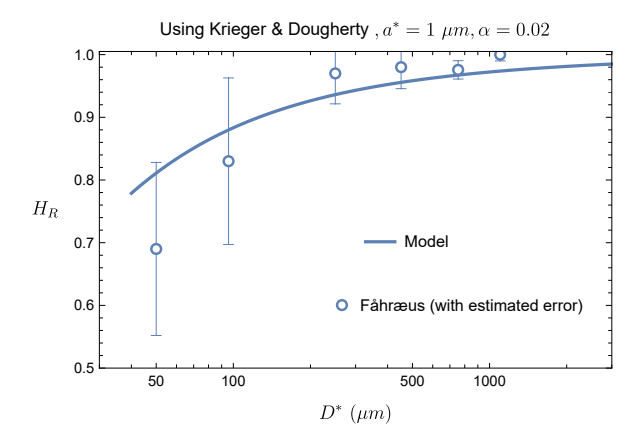


FIGURE 13. Function \mathfrak{F} versus the original Fåhræus' data. The feeding hematocrit H_F is equal to 0.405 (that one used by Fåhræus). The best agreement is obtained using the Krieger and Dougherty formula, and choosing $a^* = 1 \, \mu m$, $\alpha = 0.02$. Notice that this value of a^* is precisely half of the RBC average thickness. Notice also that with this assumption, $s_0 = 1 - 2a^*/D^*$ (see (2.24)).

where, recalling (2.6), $\eta(H_c) = f^{-1}(H_c)$ with f given by one of the classical empirical formulas listed in Table 1. Finally, coupling (3.1), (3.9) and (3.11), we get

(3.12)
$$H_R = \mathcal{F}(H_F, D^*, a^*, \alpha, f),$$

that is, a functional relation that links the relative hematocrit to H_F , α , and, through s_0 , to the vessel diameter $D^* = 2R^*$, to the inlet marginal layer thickness a^* , and, furthermore, to the specific function f in Table 1 used to evaluate $\eta(H)$.

It is now interesting to test the model against the original Fåhræus' experiment, taking into account the estimated error based on the analysis of Gaehtgens et al. [36,37], and Goldsmith et al. [40] (see Figure 11). The agreement is rather satisfactory, as it appears in Figure 13.

It is worth emphasizing the formal simplicity of the final (rigorous) formula (3.9). Indeed, since we know that for large diameters, both s_0 and $s_\infty \to 1$, it immediately follows that in that case, H_R tends to 1, regardless of the choice made for f, α and a^* in the indicated ranges. It is also interesting to check how close formula (3.9) is to the hypothesized formula (3.1). To this aim, let us define

$$\mathfrak{A}(H_F, D^*) = \frac{\partial \mathfrak{F}}{\partial H_F}, \quad \mathfrak{B}(H_F, D^*) = \hat{H}_R - \mathfrak{A}(H_F, D^*) H_F,$$

where, for simplicity, we fixed $\hat{H}_R = \mathcal{F}(H_F, D^*, 1, 0, f_{\text{B\&W}})$, $f_{\text{B\&W}}$ being the Bingham and White formula specified in Table 1. Then, we plot $\mathfrak{A}(H_F, D^*)$ and $\mathfrak{B}(H_F, D^*)$

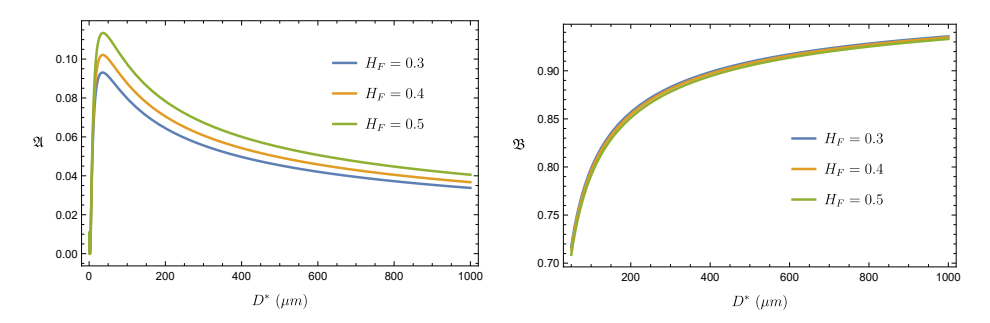


FIGURE 14. Functions $\mathfrak{A}(H_F, D^*)$ and $\mathfrak{B}(H_F, D^*)$. It appears that \mathfrak{B} is practically independent of H_F , while the variability of \mathfrak{A} with $H_F \in (0.3, 0.5)$ is less than 3%.

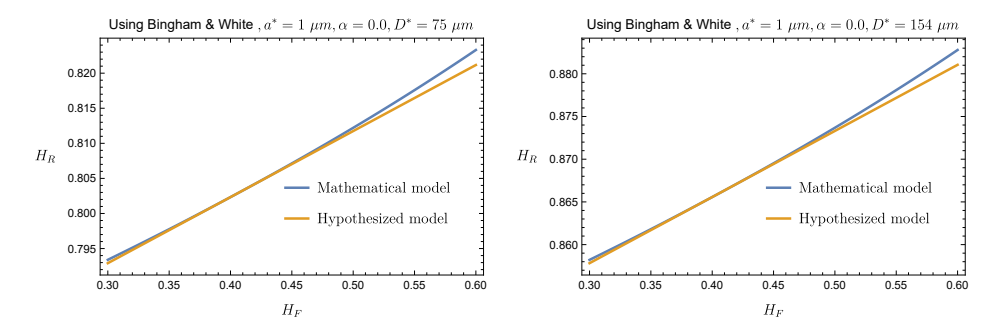


FIGURE 15. Comparison between formula (3.1) and the one provided by the mathematical model (3.12). We checked just two diameters, $D^* = 75 \,\mu\text{m}$ and $D^* = 154 \,\mu\text{m}$, respectively. Other similar choices would show the same characteristics, namely, that (3.9) provides the correct interpretation of the F effect based on the fluid dynamic equations.

versus D^* for different values of H_F . Figure 14 shows that \mathfrak{B} is practically invariant with respect to H_F , while \mathfrak{A} has a very limited variability with H_F , namely, less than 3% in the range $H_F \in (0.3, 0.5)$.

This analysis suggests that, by fixing

$$A(D^*) = \mathfrak{A}(H_{\text{phys}}, D^*), \quad B(D^*) = \mathfrak{B}(H_{\text{phys}}, D^*)$$

at $H_{\rm phys} \approx 0.4$ (a physiological value), $a^* = 1~\mu{\rm m}$ and selecting $f_{\rm B\&W}$ to evaluate η , one obtains

$$\mathfrak{F}(H_F, D^*, 1, 0, f_{\text{B\&W}}) \simeq A(D^*)H_F + B(D^*),$$

thus confirming that the relation (3.12) between H_R and H_F is, approximately, linear for all relevant diameters. Figure 15 shows, graphically, the latter conclusion.

We finally show representations of \mathfrak{F} versus D^* in which some parameters, such as f, α and a^* , are varied (see Figures 16 and 17).

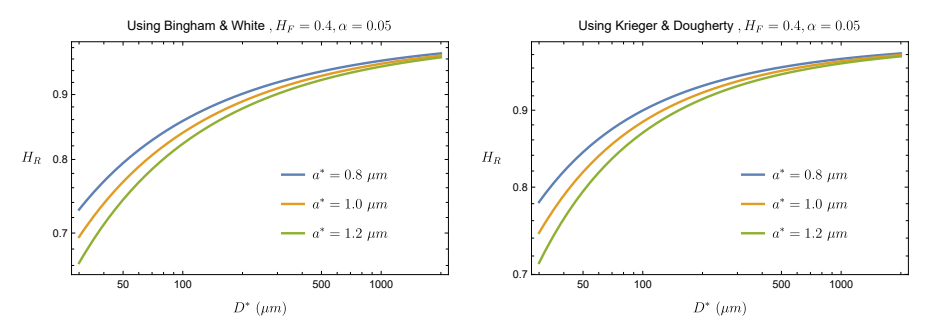


FIGURE 16. Function \mathfrak{F} versus D^* , using either Bingham and White formula (left panel) or the Krieger and Dougherty one (right panel), with $H_F=0.4$, $\alpha=0.05$ and varying a^* . The real effect of varying the latter parameter can be appreciated only through a comparison with real data.

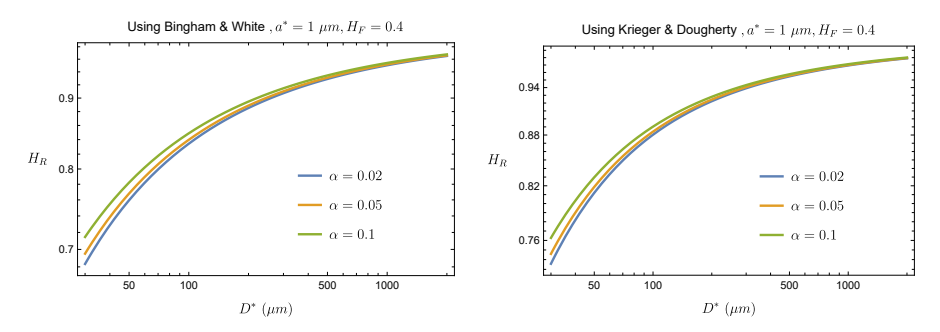


FIGURE 17. Function \mathfrak{F} versus D^* , using either Bingham and White formula (left panel) or the Krieger and Dougherty one (right panel), with $H_F=0.4$, $a^*=1~\mu\mathrm{m}$ and varying α . Also in this case, the real effect of varying the latter parameter can be appreciated only through a comparison with real data.

3.2. Comparison with the experimental data

In the sequel, we compare our model (3.12) with the data summarized in Figure 9 from Barbee and Cokelet [6]. We also compare our model with the empirical formula proposed by Pries [64] to match all the available data (at that time) for the relative hematocrit versus the vessel diameter; namely,

(3.13)
$$\frac{H_T}{H_F} = H_F + (1 - H_F) [1 + 1.7 e^{-0.35D} - 0.6 e^{-0.011D}],$$

with, as in Section 2.3, $D = D^*/D_{\text{ref}}^*$ and $D_{\text{ref}}^* = 1 \, \mu\text{m}$.

Concerning the uncertainty of the experimental data, we refer to what was already emphasized just at the end of Section 3. We recall that being in a continuum context, the experimental data are significant only for diameter above $\approx 50\,\mu m$. In the sequel, we shall see that our mathematical model fits very well Barbee's data and reasonably well those of Jendrucko and Lee.

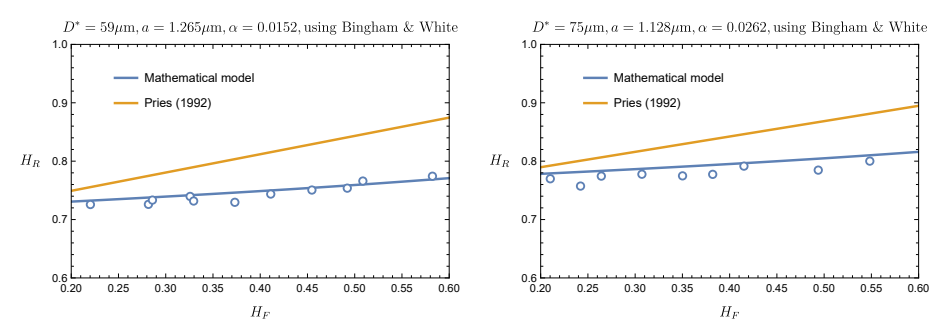


FIGURE 18. Comparison of the mathematical model (3.11), (3.12) with data extracted from [6, Figure 2] for the case $D^* = 59 \,\mu\text{m}$ and $D^* = 75 \,\mu\text{m}$. The graph provided by the Pries formula (3.13) is also shown.

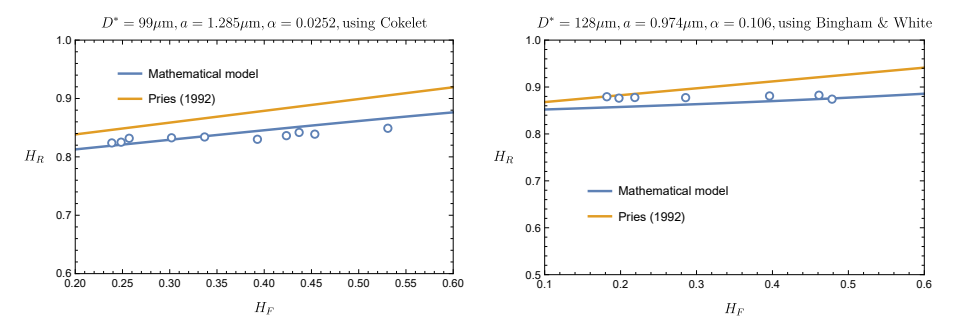


FIGURE 19. Comparison of the mathematical model (3.11), (3.12) with data extracted from [6, Figure 2] for the case $D^* = 99 \,\mu\text{m}$ and $D^* = 128 \,\mu\text{m}$. The graph provided by the Pries formula (3.13) is also shown.

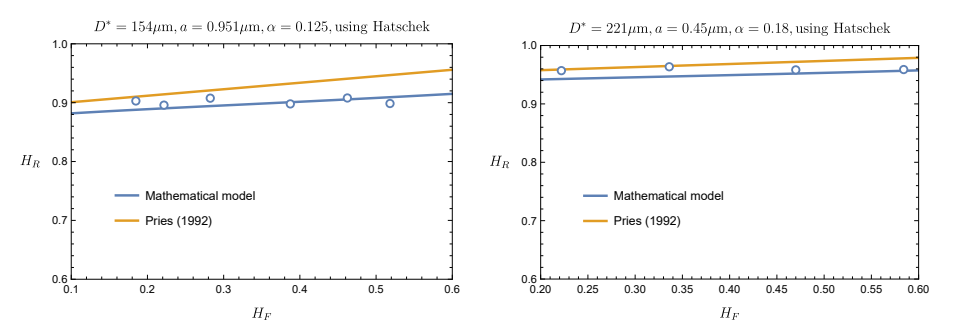


FIGURE 20. Comparison of the mathematical model (3.11), (3.12) with data extracted from [6, Figure 2] for the case $D^* = 154 \,\mu\text{m}$ and $D^* = 221 \,\mu\text{m}$. The graph provided by the Pries formula (3.13) is also shown.

To evaluate the relative viscosity as a function of H_F , required by the formula (3.11), we used the empirical formulas shown in Table 1. Figures 18, 19 and 20 show the mathematical model (3.12) (see [24]) versus the experiments by Barbee in [6]. We

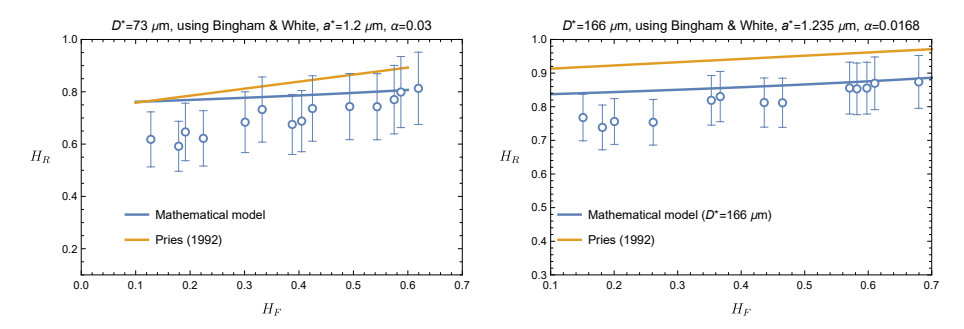


FIGURE 21. The mathematical model versus the experiments of Jendrucko and Lee [49]. The estimated error bars are included in this particular case since the agreement is not so impressive for all values of H_F as it is, indeed, in the case of Barbee's data. In any event, if $H_F > 0.3$, the agreement is still acceptable.

disregarded the case $D^*=29\,\mu\mathrm{m}$, this value being beyond the limit of applicability of the continuum hypothesis. The fitting parameters a^* , α and the formula among those listed in Table 1 are selected by using the NonlinearModelFit package in Mathematica[®], which is based on the optimization of the standard error, P-value, and t-Student test. In all cases, the obtained values for a^* and α are largely reasonable because a^* is close to 1 $\mu\mathrm{m}$ and $\alpha \leq 0.1$, as expected. The only exception seems to be the largest diameter considered by Barbee, namely, $D^*=221\,\mu\mathrm{m}$, where a^* is a little too small and α a little too large. It must be pointed out, however, that if we assume a reasonable error (2 or 3% is sufficient) in Barbee's data, both a^* and α update to more satisfying values. In drawing Figures 18, 19 and 20, we confined ourselves, for the sake of brevity, to the empirical formulas by Hatsheck [45], Cokelet [15] and Bingham and White [8]. The other formulas listed in Table 1 would have provided very similar matching with comparable values of a^* and α .

It is also interesting to check the capability of the model to reproduce the experiments by Jendrucko and Lee [49] with the cat's blood. The comparison is shown in Figure 21. We did not consider smaller values of the diameter for the same reason we did not consider the case $D^* = 29 \, \mu \text{m}$ for the human blood case. For this particular case, we have reported the estimated error in the measure of the relative hematocrit as suggested by Figure 11. Once more, we remark that our model performs better than Pries' formula.

3.3. The Fåhræus effect in small blood vessels: how does it help the heart?

In practice, we start from (2.14) and generalize the approach illustrated in Section 2.1, considering that the hematocrit of the marginal layer is H_a . Then, the dimensionless power dissipation becomes

(3.14)
$$W = s_{\infty}^4 f(H_c) + (1 - s_{\infty}^4) f(\alpha H_c).$$

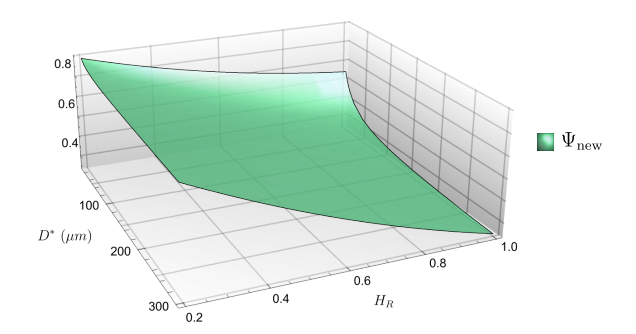


FIGURE 22. Three-dimensional representation of the dimensionless power dissipation Ψ_{new} versus D^* and H_R . The function increases either if D^* or H_R decreases. We have fixed, for simplicity, $H_F = 0.4$, $a^* = 1 \, \mu\text{m}$, $\alpha = 0.05$ and $f = f_{\text{B\& W}}$. Other choices would produce very similar graphs.

Combining now both (3.8) and (3.9) with (3.14), we obtain

$$(3.15) W = s_{\infty}^4 f\left(\frac{H_R H_F}{s_{\infty}^2 + \alpha(1 - s_{\infty}^2)}\right) + (1 - s_{\infty}^4) f\left(\frac{\alpha H_R H_F}{s_{\infty}^2 + \alpha(1 - s_{\infty}^2)}\right),$$

which rewrites as

(3.16)
$$W = \Psi_{\text{new}}(H_F, H_R, D^*, a^*, \alpha, f),$$

where Ψ_{new} generalized Ψ defined by (2.22). The behavior of Ψ_{new} is displayed in Figure 22.

An almost identical procedure leads to a generalization of (2.16) which determines the amount of perfusion in the peripheral tissues. In this case, we get

(3.17)
$$Q = s_{\infty}^4 f\left(\frac{H_R H_F}{s_{\infty}^2 + \alpha(1 - s_{\infty}^2)}\right) + (1 - s_{\infty}^4) f\left(\frac{\alpha H_R H_F}{s_{\infty}^2 + \alpha(1 - s_{\infty}^2)}\right).$$

Namely,

(3.18)
$$Q = \Psi_{\text{new}}(H_F, H_R, D^*, a^*, \alpha, f).$$

In conclusion, as in [3], we have found that the power dissipation and the blood discharge have the same functional dependence on the relevant parameters. In other words, if dissipation increases, so does perfusion.

4. VASOMOTION

Vessels of the size of venules or arterioles are equipped with smooth muscle cells that contract, reducing their lumen, with a period unrelated to cardiac pulsations. This

phenomenon was discovered in 1852 by T. W. Jones [50], who observed it in the venules of bat wings. He guessed that its purpose was to enhance blood flow. Actually, the phenomenon has different characteristics in arterioles and in venules.

While in arterioles, having no valves, the flow is substantially driven by the pressure gradient provided by the heart, in venules, vasomotion takes an important role in blood propulsion. Therefore, blood flow presents different features in the two classes of vessels and the two cases must be modeled separately.

4.1. Vasomotion in arterioles

In [27], it was first emphasized that the ratio ε between the maximal vessel radius R_o^* and its length L^* is $\ll 1$ (between 10^{-3} and 10^{-2} , for instance $R_o^* = 70 \, \mu m$, $L^* = 3 \, mm$). Based on this, an up-scaling procedure was applied to the motion equations, also exploiting the smallness (order ε^{-2}) of the ratio between the typical radial velocity (namely, the maximal velocity of the wall, $v_{\rm art}^* \simeq 2 \, \mu m/s$) and the typical longitudinal velocity ($u_{\rm art}^* \simeq 10 \, {\rm cm/s}$). Pressure p^* was rescaled as $(p^* - p_{\rm out}^*)/\Delta p^*$, with $\Delta p^* = p_{\rm in}^* - p_{\rm out}^*$. Time was rescaled by the vasomotion period T^* (typically 6 s). We omit all the calculations and we just report the conclusions. At the leading approximation order (i.e. up to order ε corrections), the longitudinal velocity profile in the vessel (with the no-slip condition at the wall) is nothing but the quasi-steady Hagen-Poiseuille quadratic profile

(4.1)
$$u^*(r^*, t^*) = \frac{1}{n^*} \frac{\Delta p^*}{L^*} \frac{R^{*2}(t) - r^{*2}}{4}.$$

Formula (4.1) emphasizes the typical value of the maximal centerline velocity

(4.2)
$$u_{\text{art}}^* = \frac{1}{\eta^*} \frac{\Delta p^*}{L^*} \frac{R_o^{*2}}{4}.$$

Thus, the flow adapts instantaneously to the radius change (as it was assumed in [61], though without justification). Here, η^* is blood viscosity ($\approx 4 \,\mathrm{mPa} \cdot \mathrm{s}$) and Δp^* is the pressure difference at the ends of the vessel (typically 8–16 mmHg, i.e. $1-2\times 10^3 \,\mathrm{Pa}$), so $\Delta p^*/L^*$ is the driving pressure gradient. For example, the above values together with $L=3 \,\mathrm{mm}$ and $R_o=50 \,\mathrm{\mu m}$ provide $u_{\mathrm{art}}^* \simeq 10-20 \,\mathrm{cm/s}$. Here, the pressure gradient turns out to be independent of the longitudinal coordinate x^* and such a gradient always overcomes the effects of vasomotion, constantly preventing flow inversion. These and other related questions regarding the blood velocity are discussed, e.g., in [2,57,76].

The associated Reynolds number is order 10^{-2} (creeping flow regime). At the same order, the radial velocity component turns out to be negligible throughout the vessel.

Assuming, for simplicity, a sinusoidal oscillation

(4.3)
$$R^*(t) = R_o^* \left[1 - \delta \left(1 - \sin \left(\frac{2\pi}{T^*} t^* \right) \right) \right],$$

where 2δ is the relative oscillation amplitude, the average discharge over a period is

$$\langle Q^* \rangle = Q_{\text{ref}}^* \langle Q \rangle$$

where

(4.5)
$$Q_{\text{ref}}^* = \frac{\pi \Delta p^*}{8L^* n^*} R_o^{*4}, \quad \langle Q \rangle = 1 - 4\delta + 9\delta^2 - 10\delta^3 + \frac{35}{8} \delta^4.$$

The average dimensionless discharge over a period $\langle Q \rangle$ is decreasing and less than 1 for $0 < \delta \le 0.5$, showing that the discharge is reduced with respect to the vessel rest configuration ($\delta = 0$) and the reduction increases as the oscillation amplitude increases, down to $\approx 27\%$ for $\delta = 0.5$ (see Figure 23).

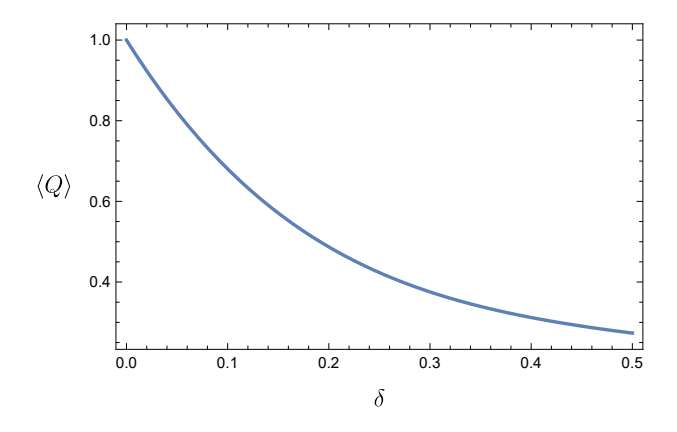


FIGURE 23. Average dimensionless discharge over a period.

4.2. Combining vasomotion in arterioles with the FL effect

In this section, we examine vasomotion combined with the FL effect. In the previous section, we have highlighted that the arterioles wall oscillations caused by vasomotion reduces the overall flow rate, while the FL effect acts in the opposite direction, increasing both discharge and energy dissipation (see Section 2.1). It is interesting to analyze the combination of the two phenomena to understand the effect they have on the overall flow.

Recalling (2.13), the dimensionless discharge is

(4.6)
$$Q(t) = s_{\infty}^{4} + \mathfrak{G}(\alpha, \eta_{c})(R^{4}(t) - s_{\infty}^{4}),$$

where Q^* has been rescaled with $\frac{\pi \Delta p^* R_o^{*4}}{8L^* \eta_c^*}$, $R(t) = R^*(t)/R_o^*$, with $R^*(t)$ given by (4.3), $s_\infty = s_\infty^*/R_o^*$, and where, recalling (2.27),

(4.7)
$$\mathfrak{G}(\alpha, \eta_c) = \frac{\eta_c^*}{\eta_a^*} = \frac{\eta_c}{1 + \alpha(\eta_c - 1)},$$

with $\eta_c = \eta_c^*/\eta_p^*$. Following now the same procedure illustrated in Section 2.2, we express s_{∞} in terms of s_o , $\mathfrak{E}(\alpha, \eta_c)$ and R(t), so we get

$$(4.8) \ \langle Q \rangle = \int_0^1 \left[\frac{s_o^4 (1 - \mathfrak{G}(\alpha, \eta_c))}{\left(1 + \sqrt{\left(1 - \frac{s_o^2}{R^2} \right) \left[1 - \frac{s_o^2}{R^2} \left(1 - \frac{1}{\mathfrak{G}(\alpha, \eta_c)} \right) \right]} \right)^2} + \mathfrak{G}(\alpha, \eta_c) R^4 \right] dt.$$

We remark that $\langle Q \rangle$ is a function of a^* , the vessel diameter in the unstressed configuration $D_0^* = 2R_o^*$, the oscillation amplitude δ , and, through \mathfrak{E} , of α and η_c . We also remark that $\langle Q \rangle$ does not depend on α when $a^* \to 0$, as physically expected. Indeed, recalling that $s_o^* = R^* - a^*$, with R^* given by (4.3), we have $s_o = R(t) - a$, with $a = a^*/R_o^*$. Therefore, if $a^* \to 0$, we get $s_o = R(t)$ and (4.8) reduces to $\langle Q \rangle = \int_0^1 R^4(t) \, dt$. We also point out that if $a^* \to 0$, η_c is to be understood as the viscosity (relative to plasma) of the blood in the entire vessel. It should be noted that the case $a^* = 0$ is purely academic, as it is equivalent to the absence of a marginal layer (poor in erythrocytes), which, as experimental observations [39, 52, 74] confirm, is in fact always present.

We point out that, given the vessel diameter D_o^* , $\langle Q \rangle$ depends on a^* , δ and both α and η_c through $\mathfrak E$. The three surfaces in Figure 24 were obtained by choosing $\eta_c=3.5$ and three values for a^* , namely, $a^*=0.5,1,1.5\,\mu\mathrm{m}$, and expressing $\langle Q \rangle$ in terms of

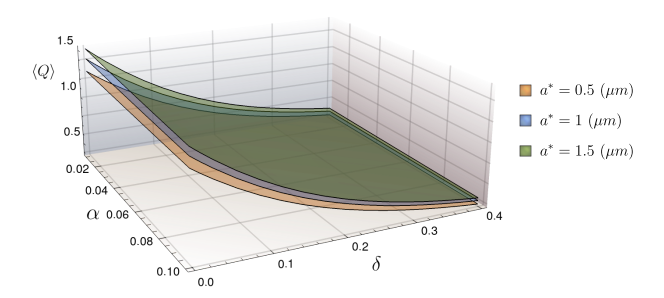


FIGURE 24. Average discharge $\langle Q \rangle$ for $D_0^* = 200 \, \mu \mathrm{m}$ and $\eta_c = 3.5$. In this case, $\langle Q \rangle$ depends only on δ and α since for fixed η_c , $\mathfrak E$ is a function of α only. The effect of varying α between 0.01 and 0.1 appears to be negligible for all values of $a^* \neq 0$. Of course, as remarked in the text, if $a^* \to 0$, the average discharge does not depend on α , where $\langle Q \rangle = \int_0^1 R^4(t)$.

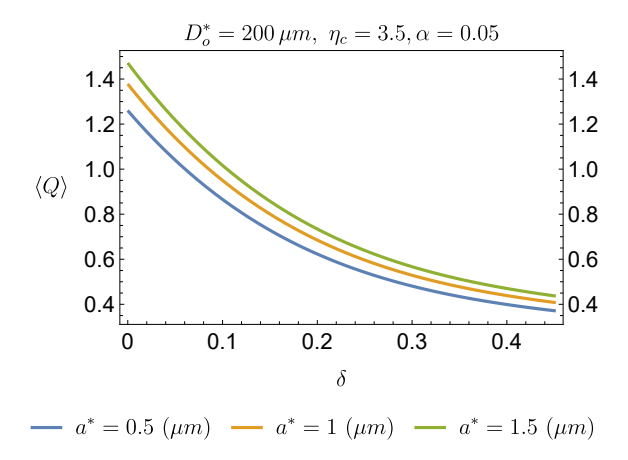


FIGURE 25. The behavior of $\langle Q \rangle$ as a function of δ with the FL effect $(a^* > 0)$. Notice that when $a^* \to 0$, $\langle Q \rangle$ identifies with the profile shown in Figure 23, as expected.

 α and δ . We first find that $\langle Q \rangle$ is a decreasing function of δ and conclude, as in [27], that wall oscillations (i.e. vasomotion) hinder blood flow in a single arteriole. However, we also find that $\langle Q \rangle$ increases significantly when a^* increases, i.e. when the FL effect is at work. Although not shown in the other figures, the same behavior of $\langle Q \rangle$ also occurs for other values of η_c between 2 and 5.

A clearer insight into $\langle Q \rangle$ is given in Figure 25 where we still consider $\eta_c=3.5$, $D_0^*=200\,\mu\mathrm{m}$ and have set $\alpha=0.05$, so that $\mathfrak{E}\simeq 3.11$. The diagrams in Figure 25 show that $\langle Q \rangle$ decreases with increasing oscillation amplitude δ , but when the FL effect is taken into account (i.e., $a^*\geq 1\,\mu\mathrm{m}$), the reduction of $\langle Q \rangle$ is significantly attenuated. For example, for $\delta=0.4$, the value of $\langle Q \rangle$ for $a^*=1\,\mu\mathrm{m}$ (a quite reasonable value) is about 10% larger than for $a^*=0.5\,\mu\mathrm{m}$, confirming the role of the FL effect in attenuating the effect of vasomotion in arterioles.

It is interesting to compute the mechanical power dissipated in the whole vessel W^* . Using formula (2.14) and normalizing W^* with $\frac{\pi}{8} \frac{R_0^{*4} \Delta P^{*2} T^*}{\eta_c^* L^*}$, it turns out that (see [23] for more details)

$$(4.9) \langle W \rangle = \langle Q \rangle.$$

We can conclude that the minimum energy dissipation, i.e. the minimum mean discharge, occurs when $a^* \to 0$, namely, when the FL effect does not play any role. This is in agreement with the results of Section 2.1, where it was shown that the FL effect increases both the mechanical dissipation and the discharge. In other words, it is confirmed that the increase of discharge is necessarily accompanied by a proportional increase of energy dissipation.

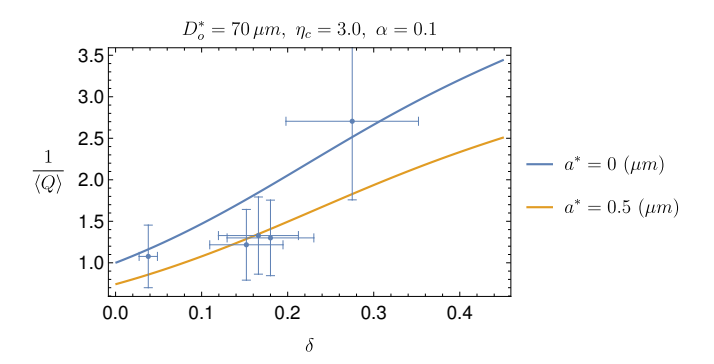


FIGURE 26. The apparent hydraulic resistance $1/\langle Q \rangle$ according to the mathematical model (4.8), either considering the FL effect ($a^*=0.5~\mu m$) or not ($a^*=0~\mu m$), when $D_o^*=70~\mu m$, $\alpha=0.1$ and $\eta_C=3.0$. The data points are taken from [42] (nonpregnant rats case). Even considering an uncertainty of 30% of the measured values, the correction induced by the FL effect largely improves the fit with experimental data.

4.3. Comparison with the experimental data by Gratton et al. [42]

The literature on vasomotion in arterioles is less abundant than that in venules. We selected the data presented in [42] to validate the conclusions of the previous section. First of all, it is important to emphasize that data presented in [42] adopt some different conventions. Indeed, the parameter r_0 , used therein as a scaling factor, is the mean value of the radius, while we preferred to use its maximum. Moreover, Figure 6 in [42] shows the relative resistance as a function of percent maximum constriction induced by phenylephrine, instead of the dimensionless amplitude. The latter is obtained as a function of the percent maximum constriction and shown in [42, Figure 5]. Therefore, to use the experimental data in [42], we needed to suitably rearrange them. Furthermore, Gratton et al. consider both pregnant and nonpregnant rats. Here, we confined ourselves to the nonpregnant case only. Finally, it must be stressed that the data presented in [42, Figures 5 and 6] appear rather spread around the nonlinear regression curve, suggesting an error of 30% at least. Figure 26 shows the data points (with their error bars) and the average relative hydraulic resistance obtained from model (4.8) for two different values of a^* . We notice that the curve with $a^* \neq 0$ (FL effect enforced) appears more satisfactory with respect to the case $a^* = 0$, in which the FL effect plays no role. We also remark that the value $a^* = 0.5 \,\mu\text{m}$ is consistent with the real size of RBCs in the species considered.

(7) Phenylephrine (PE), a direct-acting α 1-adrenoceptor agonist, is primarily used clinically as a vasopressor to increase blood pressure.

4.4. Modeling a network of arterioles

We have seen that (see Figure 23) that vasomotion in arterioles is not advantageous for the blood flow rate. Thus, a legitimate question arises: what is the physiological reason of vasomotion in arterioles? We started from the experiments of Lapi et al. [56] aimed at characterizing the geometrical arrangement of a hamster skeletal muscle arteriolar network and assessing the *in vivo* rhythmic diameter changes of arterioles to clarify regulatory mechanisms of the capillary perfusion. These experiments have suggested the idea that the results of Lapi et al. could be used in our model for the discharge, provided we extend our modeling approach from a single vessel to a network of arterioles. Indeed, in [23], we have shown that the oscillations at different frequencies of the vessels afferent to an arterioles tree can periodically convey, due to the appropriate phase shift, the blood flow towards one sector rather than another.

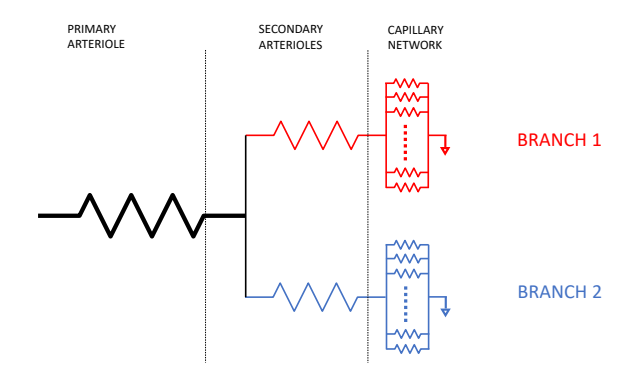


FIGURE 27. Schematic representation of a vessel network: a single arteriole is bifurcating into two smaller arterioles, which, in turn, branch into a capillary network. Blood is flowing from left to right.

The leading idea is to describe the network as a simple electric circuit⁸ with resistors whose ends have the same voltage since we can safely assume that the pressure at the end of the capillary networks is the same. The purpose of the model is to compute the flow rates in branches 1 and 2 of Figure 27 during one period of oscillation of the mother vessel (primary arteriole), and to show that, through an appropriate phase shift between the oscillations of the secondary vessels radius, the blood flow can be periodically and unequally distributed in the two branches.

(8) The idea of modeling the network as a highly simplified electrical circuit is not new; see [16].

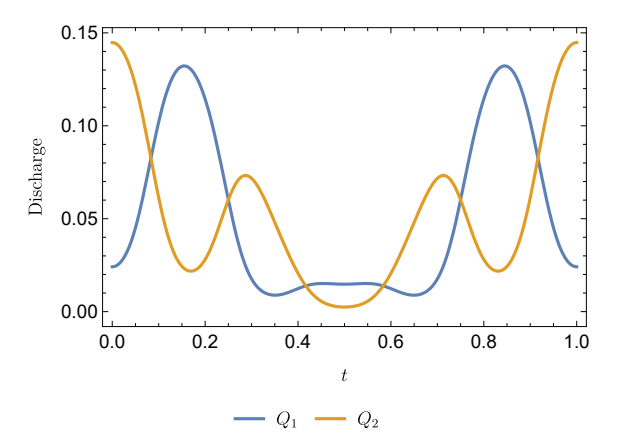


FIGURE 28. Dimensionless discharges Q_1 and Q_2 in the two bifurcating branches for a π phase shift and equal hydraulic resistances.

Here, we do not enter into the mathematical details of the model (we refer the interested readers to [23]). Indeed, we just show in Figure 28 the dimensionless discharges Q_1 , Q_2 in the two bifurcating branches when the phase shift is π (different branches oscillate, generally, with different frequencies and phase shifts). If the pressure difference at the ends of the two branches is the same, the flow rate depends on the instantaneous hydraulic resistance of the individual branch.

In Figure 28, the hydraulic resistances of the two branches are the same. The plots clearly highlight that the flow is periodically directed to branch 1 and branch 2. Such an effect is not canceled even if the hydraulic resistances are different.

Simulations are carried out using real data from the work of Lapi et al. [56], assuming that the hydraulic resistances of the capillary networks at the end of the two branches are comparable with each other.

The mathematical model confirms the experiments by Lapi et al. [56], namely, that the capillary blood flow was modulated by changes in the diameter of terminal arterioles penetrating within the skeletal muscle fibers, facilitating the redistribution of blood flow according to the metabolic demands of tissues.

4.5. Venules equipped with an inlet and an outlet valve

Adopting reference values for pressure and velocities suitable to the venules situation, the rescaling procedure carried out on the fundamental governing equations leads to completely different conclusions for the arterioles case. For instance, the radial velocity component $v^*(r^*,t^*)$ is now playing an important role. The pressure difference $\Delta p^* = p_{\rm in}^* - p_{\rm out}^*$ is now of the order of 100 Pa, comparable to the average pressure

 $p_{\rm ven}^*$ in the venule. As a consequence, competition arises between the two driving mechanisms which will be responsible for the activation of the valve. Let us point out the main characteristics of this complex flow.

- (i) Differently from the case of arterioles, where pressure has a linear dependence on the longitudinal coordinate x^* , here, the second derivative of pressure with respect to x^* is not zero and is not constant in time.
- (ii) The valves placed at the ends of the venule open or close to ensure that the longitudinal blood velocity never becomes negative, preventing backflow. Mathematically, this behavior is expressed by boundary conditions including unilateral constraints (Signorini-type conditions [51]).

Much care must be put in selecting the reference quantities for pressure and velocity, providing the natural scale for the dimensionless reformulation of the differential equations at the leading order in ε . A natural choice for the wall velocity $v_{\rm ven}^*$ is $4 \, \delta \, R_o^* / T^*$, while the expected characteristic longitudinal velocity is $u_{\rm ven}^* = v_{\rm ven}^* / \varepsilon$. The peristaltic pressure is now rescaled by

$$p_{\text{ven}}^* = \frac{\eta^*}{R_o^*} \frac{v_{\text{ven}}^*}{\varepsilon^2} = 4\delta \frac{\eta^*}{T^*} \frac{1}{\varepsilon^2}.$$

For $\delta = 0.25$, $\eta^* = 4$ mPa·s, $T^* = 6$ s, $1/\varepsilon^2 = 10^5$, we find 133 Pa, thus of the same order as Δp^* . At the venule inlet and outlet boundaries, some peculiar conditions must be imposed representing the valve action:

At
$$x^* = 0$$
 (inlet),

- either $\partial p^*/\partial x^* = 0$ (that is, the valve is closed) or $p^* = p_{\text{in}}^* = \Delta p^* + p_{\text{out}}^*$ (that is, the valve is open),
- $\partial p^*/\partial x^* \le 0$ (forbidding backflow),
- $p^* \geq p_{\text{in}}^*$.

At
$$x^* = L^*$$
 (outlet),

- either $\partial p^*/\partial x^* = 0$ (that is, the valve is closed) or $p^* = p_{\text{out}}^*$ (that is, the valve is open),
- $\partial p^*/\partial x^* \le 0$ (forbidding backflow),
- $p^* \ge p_{\text{out}}^*$.

These conditions model the interplay between the flow and the valves: a valve open makes pressure equal to the outer pressure, and that occurs if the flow is running in the allowed direction (negative pressure gradient). When a valve closes, the longitudinal velocity vanishes $(\partial p^*/\partial x^* = 0)$ and pressure is allowed to evolve freely (above the inlet value at the entrance, below the outlet value at the exit). Here too, we skip all

calculations (see [25], for details) and jump to the conclusions, valid at the main order approximation, adopting the original dimensional variables. Pressure is no longer linear in x^* but it exhibits a time-dependent, constant in-space curvature:

(4.10)
$$\frac{\partial^2 p^*}{\partial x^{*2}} = 16\eta^* \frac{\dot{R}^*}{R^{*3}},$$

where the superimposed dot represents differentiation with respect to time.

Equation (4.10) comes from the combination of the remaining governing differential equation at the leading order, which we here write in the dimensional form

(4.11)
$$u^* = -\frac{1}{n^*} \frac{\partial p^*}{\partial x^*} \frac{R^{*2} - r^{*2}}{4},$$

(4.12)
$$\frac{\partial u^*}{\partial x^*} + \frac{1}{r^*} \frac{\partial (r^*v^*)}{\partial r^*} = 0.$$

We just differentiate (4.11) w.r.t. x^* , insert the result into (4.12) and then integrate w.r.t. r^* , remembering that, at the considered approximation order, p^* does not depend on r^* , and that $v^*(x^*, R^*(t^*), t^*) = \dot{R}^*(t^*)$. It is remarkable, by the way, that now the radial component of the velocity appears at the leading order approximation. The pressure profile can be found by exploiting the boundary conditions, and it is different in the compression and the expansion phase of the vessel oscillation. It is useful to introduce a quantity, which we may call *vasomotion pressure*

(4.13)
$$p_{\text{vas}}^*(t^*) = 8\eta^* L^{*2} \frac{\left|\dot{R}^*(t^*)\right|}{R^{*3}(t^*)}.$$

This pressure discriminates the valve state by comparison with Δp^* at each time instant. It is important to remark that $p_{\text{vas}}^*(t^*)$ vanishes when $\dot{R}^*=0$, but during the wall oscillation, it can reach values larger than Δp^* if vasomotion is strong enough. In Figure 29, we have reported p_{vas}^* and Δp^* to highlight the intervals of engagement/noengagement of the inlet-outlet valves. Notice that if $p_{\text{vas}}^*(t^*)$ never exceeds Δp^* , then valves are never engaged, thus becoming unnecessary, as it happens in arterioles.

- (A) Compression phase ($\dot{R}^* < 0$). Here and in the sequel, $x = x^*/L^*$. The outlet valve (x = 1) is open. We distinguish two cases:
- (a) $p_{\text{vas}}^* < \Delta p^*$. Then, the inlet valve is open and the pressure profile is $p_{\text{comp}}^*(x,t^*) = p_{\text{vas}}^*(t^*)(x-x^2) \Delta p^*(x-1), \quad \left(p^*(0,t^*) = \Delta p^* + p_{\text{out}}^* = p_{\text{in}}^*\right).$
- (b) $p_{\text{vas}}^* > \Delta p^*$. Then, the inlet valve is closed and the pressure profile is

$$p_{\text{comp}}^*(x, t^*) = p_{\text{vas}}^*(t^*)(1 - x^2), \quad (p^*(0, t^*) = p_{\text{vas}}^*(t^*) + p_{\text{out}}^* > p_{\text{in}}^*).$$

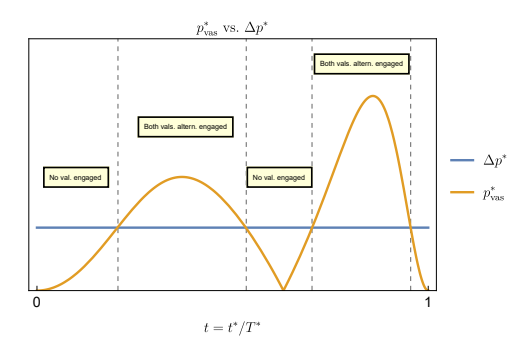


FIGURE 29. Time intervals of engagement/no-engagement of the inlet-outlet valves as a function of the difference $\Delta p^* - p_{\text{vas}}^*$ (the value of Δp^* is exaggerated for visualization purposes).

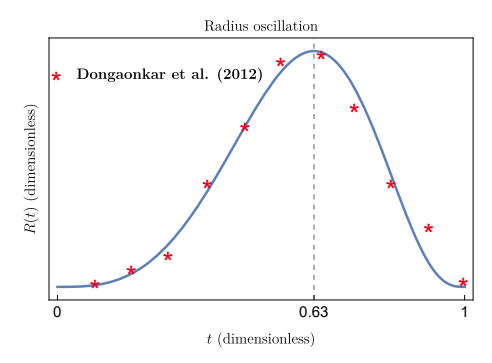


FIGURE 30. Experimentally measured radius oscillation vs. the approximating function (4.14). The maximum of R is in $t_{\text{max}} \approx 0.63$. The expansion phase occurs for $t \in (0, t_{\text{max}})$, the compression one for $t \in (t_{\text{max}}, 1)$.

- (B) Expansion phase ($\dot{R}^* > 0$). The inlet valve (x = 0) is open. Here too we have two cases:
- (c) $p_{\text{vas}}^* < \Delta p^*$. Then, the outlet valve is open and the pressure profile is $p_{\text{exp}}^*(x,t^*) = p_{\text{vas}}^*(t^*)(x^2 x) \Delta p^*(x-1) + p_{\text{out}}^*, \quad (p^*(1,t) = p_{\text{out}}^*).$
- (d) $p_{\text{vas}}^* > \Delta p^*$. Then, the outlet valve is closed and the pressure profile is $p_{\text{exp}}^*(x, t^*) = p_{\text{vas}}^*(t^*)(x^2 2x) + \Delta p^* + p_{\text{out}}^*, \quad (p^*(1, t^*) \le p_{\text{out}}^*).$

In [27], the vasomotion law $R^*(t^*)$ experimentally observed by Dongaonkar et al. [18] in the bat wing was very closely approximated by

(4.14)
$$\frac{R^*(t^*)}{R_o^*} = 2.37 \left(\frac{t^*}{T^*}\right)^3 \left(1 - \left(\frac{t^*}{T^*}\right)^3\right)^3 + 0.75,$$

repeated periodically with $R_o^* = 70 \, \mu \text{m}$ and period $T^* = 6 \, \text{s}$, reaching the maximum $(R^* = R_o^*)$ at the time $\approx 0.63 \, T^*$ (see Figure 30).

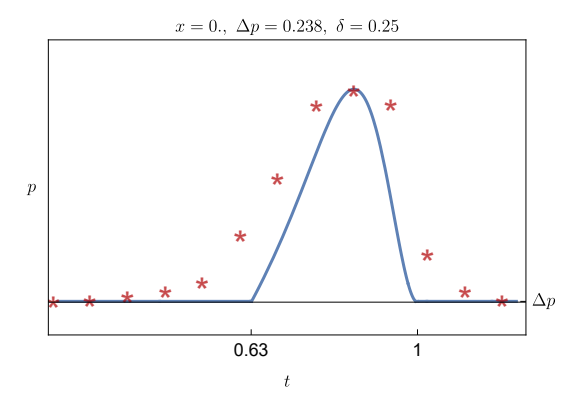


FIGURE 31. Best fit in x=0 of the dimensionless luminal pressure measured by Dongaonkar et al. (see [18, Figure 5]), and its rescaled dimensionless version, [25, Figure 6]. Here, $\Delta p=0.238$ and $\delta=0.25$. The pressure remains above Δp as long as $t\in(t_{\max},1)$ (compression phase) (see Figure 30). During this interval, the inlet valve is closed, and the outlet valve is open. The flat branches of the graph correspond to the situation in which both valves are open ($p|_{x=0}=\Delta p+p_{\text{out}}$) and $p|_{x=1}=p_{\text{out}}$).

The model above provided a good fit with the experimentally measured pressure, as shown in Figure 31.

It can be noticed that the fit is excellent near the pressure peak, but that pressure is underestimated during the increase and decrease phases. Such a discrepancy was addressed in the paper [9] starting with the remark that the Signorini-type boundary conditions at the location of the valves (x=0,x=1) can be interpreted as a stepwise relationship between p (dimensionless) and the (dimensionless) pressure gradient $G=\partial p/\partial x$. Indeed, in x=0 as long as $\partial p/\partial x<0$ (blood flowing in), the pressure equals the given inlet pressure, while p is free to increase when the valve closes $(\partial p/\partial x=0)$. The dimensionless pressure gradient G is never allowed to become positive. Figure 32 provides a representation as a graph of the alternatives related to the Signorini-type conditions.

A model variant consists of replacing these sharp graphs with the respective hyperbolic approximations,

(4.15)
$$p_{\text{in}} = \Delta p \left(1 - \frac{n}{G} \right),$$
$$p_{\text{out}} = \frac{m}{G}, \quad \text{for } x = L,$$

where n and m are positive numbers which can be associated with the speed of the valve's action. This modification yields a better fitting with n=100, m=50 (see [9, Figure 2]). Lower values of n, m could effectively represent the flow in pathological case, like valve incontinence.

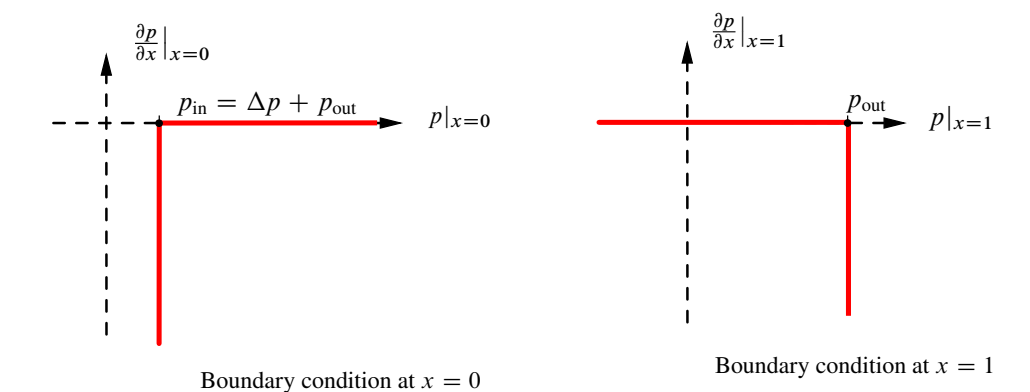


FIGURE 32. Pressure gradient vs. pressure at the inlet x = 0 and outlet x = 1 ends.

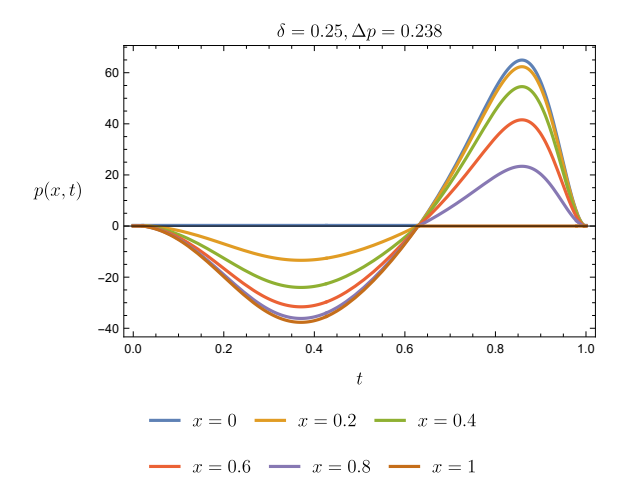


FIGURE 33. Pressure profile versus time at different distances from the inlet valve for $\Delta p = 0.238$ (dimensionless) and $\delta = 0.25$. We notice the closure of the outlet valve (at x = 1) when $t \in (0,0.63)$ and the closure of the inlet valve at x = 0 when $t \in (0.63,1)$. In this case, p_{vas} is less than Δp only for very small time intervals close to t = 0, t = 0.63 and t = 1.

Figure 33 shows the pressure profile in six different longitudinal locations along the vessel when the boundary conditions are of the Signorini-type (see Figure 32). Figures 34 and 35 show, respectively, the pressure profiles versus time at x=0 and x=1, in the expansion phase, i.e., $t \in (0,0.63)$ and the compression phase, i.e., $t \in (0.63,1)$ (see Figure 30). The dimensionless value of Δp needed to fit the experimental curve by Dongaonkar et a. [18] is rather small, compared to the dimensionless values reached by p_{vas} (see Figure 31). This implies that p_{vas} becomes lower than Δp only for negligible time sub-intervals of (0,1). Therefore, in this specific case, both valves are practically always alternatively engaged.

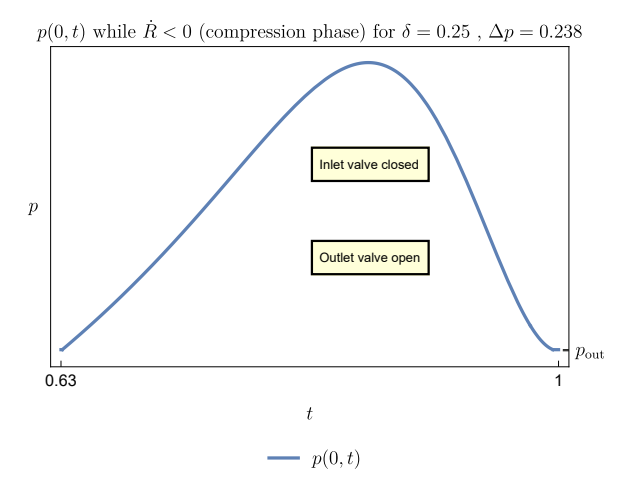


FIGURE 34. Pressure profile versus time at x=0 during the compression phase (the outlet valve is open) for $\Delta p=0.238$ (dimensionless) and $\delta=0.25$ (see Figure 33). The compression phase occurs for $t\in(0.63,1)$. In this case, $p_{\rm vas}$ is less than Δp only for very small time sub-intervals close to t=0.63 and t=1.

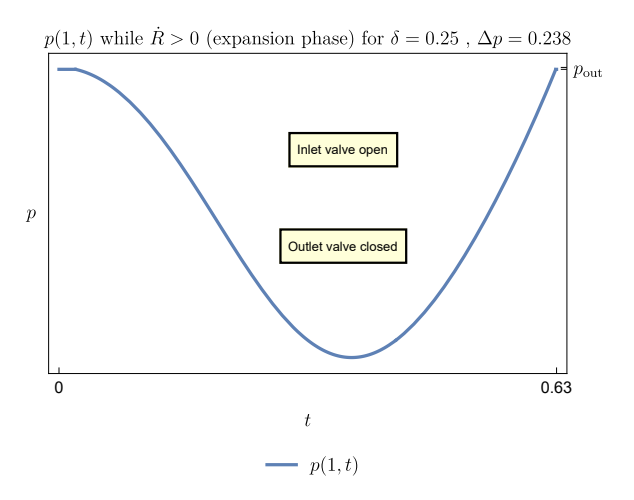


FIGURE 35. Pressure profile versus time at x=1 during the expansion phase (the inlet valve is open) for $\Delta p=0.238$ and $\delta=0.25$. The expansion phase occurs for $t\in(0,0.63)$. In this case, p_{vas} is less than Δp only for very small time sub-intervals close to t=0 and t=0.63.

5. Conclusion

We have discussed a number of recent findings on some particular phenomena in blood circulation in small vessels (in the range of 50–500 µm), namely, the so-called F and FL effects in addition to vasomotion. All these phenomena were discovered a long time

ago but lacked a rationale based on the fundamental laws of dynamics of fluids and fluid-solid mixtures. Besides filling this gap, the additional aim pursued here was to provide an interpretation of their physiological relevance for improving tissue perfusion with respect to the aforementioned studies and to point out that some of the assumptions made in the past on this topic were not correct. We also investigated the combination of the FL effect with vasomotion and emphasized the resulting benefit.

| Symbol | Unit | Meaning |
|----------------|-------------------------------|---|
| R^* | m | Vessel radius |
| D^* | m | Vessel diameter |
| η^* | Pa s | Blood viscosity |
| L^* | m | Vessel length |
| p^* | Pa | Blood pressure |
| H | _ | Hematocrit |
| \mathbb{T}^* | Pa | Shear stress tensor |
| \mathbb{D}^* | s^{-1} | Shear rate tensor |
| u^* | $\mathrm{m}\mathrm{s}^{-1}$ | Longitudinal blood velocity |
| <i>s</i> * | m | Radius of the RBCs rich core |
| v^* | ${\rm ms^{-1}}$ | Radial blood velocity |
| f | _ | Literature empirical formula for viscosity |
| V^* | m^3 | Vessel volume |
| W^* | $\mathrm{J}\mathrm{s}^{-1}$ | Dissipated power |
| Q^* | $\mathrm{m}^3\mathrm{s}^{-1}$ | Volumetric flow rate |
| T^* | s | Oscillation period |
| G | _ | Dimensionless pressure gradient |
| α | _ | Fitting parameter |
| ξ* | J | Mechanical energy dissipated in a cycle |
| a* | m | Marginal layer thickness at the vessel entrance |

Table 3. List of symbols used throughout the paper. Here, only SI units are indicated although, occasionally, various alternative units or sub-units are used. If a symbol appears in the text with the superscript "*", it means that the corresponding quantity is meant to be dimensional; otherwise, it must be considered dimensionless.

REFERENCES

- [1] D. Ambrosi A. Quarteroni G. Rozza (eds.), *Modeling of physiological flows*. MSA. Model. Simul. Appl. 5, Springer, Milano, 2012.
- [2] K.-E. Arfors D. Bergqvist M. Intaglietta B. Westergren, Measurements of blood flow velocity in the microcirculation. *Ups. J. Med. Sci.* **80** (1975), no. 1, 27–33.
- [3] M. ASCOLESE A. FARINA A. FASANO, The Fåhræus–Lindqvist effect in small blood vessels: how does it help the heart? *J Biol Phys* **45** (2019), no. 4, 379–394.
- [4] F. AZELVANDRE C. OIKNINE, Effet Fåhræus et effet Fåhræus–Lindqvist: résultats expérimentaux et modèles théoriques. *Biorheology* 13 (1976), no. 6, 325–335.
- [5] J. H. BARBEE, The flow of human blood through capillary tubes with inside diameters between 8.7 μm and 221 μm. Ph.D. thesis, California Institute of Technology, Pasadena, 1971.
- [6] J. H. Barbee G. R. Cokelet, The Fåhræus effect. Microvasc. Res. 3 (1971), no. 1, 6-16.
- [7] N. Bessonov A. Sequeira S. Simakov Y. Vassilevskii V. Volpert, Methods of blood flow modelling. *Math. Model. Nat. Phenom.* 11 (2016), no. 1, 1–25. Zbl 1384.92024 MR 3452632
- [8] E. C. Bingham G. F. White, The viscosity and fluidity of emulsions, crystallin liquids and colloidal solutions. *J. Am. Chem. Soc.* **33** (1911), no. 8, 1257–1275.
- [9] M. CARDINI A. FARINA A. FASANO A. CAGGIATI, Blood flow in venules: A mathematical model including valves inertia. *Veins and Lymphatics* 8 (2019), no. 1, 59–62.
- [10] R. Chambers, Vasomotion in the hemodynamics of the blood capillary circulation. *Ann. N. Y. Acad. Sci.* **49** (1948), no. 4, 549–552.
- [11] K. Chandran I. S. Dalal K. Tatsumi K. Muralidhar, Numerical simulation of blood flow modeled as a fluid-particulate mixture. *J. Non-Newton. Fluid Mech.* **285** (2020), article no. 104383. MR 4149263
- [12] S. E. Charm G. S. Kurland, *Blood flow and microcirculation*. John Wiley & Sons, New York, 1974.
- [13] R. Chebbi, Dynamics of blood flow: modeling of the Fåhræus–Lindqvist effect. *J. Biol. Phys.* **41** (2015), no. 3, 313–326.
- [14] R. Chebbi, A two-zone shear-induced red blood cell migration model for blood flow in microvessels. *Front. Phys.* **7** (2019), article no. 206.
- [15] G. R. Cokelet, *The rheology of human blood*. Ph.D. thesis, MIT Department of Chemical Engineering, 1963.
- [16] M. J. Davis, Control of bat wing capillary pressure and blood flow during reduced perfusion pressure. Am. J. Physiol. 255 (1988), H1114–H1129.
- [17] C. A. Dawson, Role of pulmonary vasomotion in physiology of the lung. *Physiol. Rev.* **64** (1984), no. 2, 544–616.

- [18] R. M. Dongaonkar et al., Blood flow augmentation by intrinsic venular contraction in vivo. Am. J. Physiol. Regul. Integr. Comp. Physiol. 302 (2012), no. 12, R1436–R1442.
- [19] A. ELHANAFY Y. ABUOUF S. ELSAGHEER S. OOKAWARA S. NADA M. AHMED, Effect of micro-vessel stenosis severity and hematocrit level on red blood cell dynamics and platelet margination: a numerical study. *Internat. J. Engrg. Sci.* **205** (2024), article no. 104155. Zbl 07967292 MR 4801486
- [20] C. R. Ethier C. A. Simmons, *Introductory biomechanics: From cells to organisms*. Camb. Texts Biomed. Eng., Cambridge University Press, Cambridge, 2007.
- [21] R. Fåhræus, The suspension stability of the blood. Physiol. Rev. 9 (1929), no. 2, 241–274.
- [22] R. Fåhræus T. Lindqvist, The viscosity of the blood in narrow capillary tubes. *Am. J. Physiol.* **96** (1931), no. 3, 562–568.
- [23] A. FARINA A. FASANO F. Rosso, Modeling of vasomotion in arterioles. J. Theoret. Biol. 544 (2022), article no. 111124. Zbl 1491.92046 MR 4412720
- [24] A. FARINA A. FASANO F. Rosso, A theoretical model for the Fåhræus effect in medium-large microvessels. J. Theoret. Biol. 558 (2023), article no. 111355. Zbl 1504.92039 MR 4513891
- [25] A. FARINA L. Fusi A. FASANO A. CERETANI F. Rosso, Modeling peristaltic flow in vessels equipped with valves: implications for vasomotion in bat wing venules. *Internat. J. Engrg. Sci.* 107 (2016), 1–12. Zbl 1423.76518 MR 3539706
- [26] A. Farina F. Rosso A. Fasano, A continuum mechanics model for the Fåhræus–Lindqvist effect. *J. Biol. Phys.* **47** (2021), no. 3, 253–270.
- [27] A. Fasano A. Farina A. Caggiati, Modeling vasomotion. Rev. Vasc. Med. 8 (2017), 1–4.
- [28] A. Fasano A. Farina J. Mizerski, Modeling blood flow in fenestrated capillaries and ultrafiltration in kidney glomeruli. *Adv. Math. Sci. Appl.* **23** (2013), no. 2, 319–337. Zbl 1301.92018 MR 3236621
- [29] A. FASANO A. SEQUEIRA, *Hemomath: The mathematics of blood*. MSA. Model. Simul. Appl. 18, Springer, Cham, 2017. Zbl 1385.92001 MR 3727113
- [30] D. A. Fedosov B. Caswell A. S. Popel G. E. Karniadakis, Blood flow and cell-free layer in microvessels. *Microcirculation* 17 (2010), no. 8, 615–628.
- [31] L. Formaggia D. Lamponi A. Quarteroni, One-dimensional models for blood flow in arteries. *J. Engrg. Math.* 47 (2003), no. 3-4, 251–276. Zbl 1070.76059 MR 2038983
- [32] L. FORMAGGIA A. QUARTERONI A. VENEZIANI (eds.), Cardiovascular mathematics. Modeling and simulation of the circulatory system. MSA. Model. Simul. Appl. 1, Springer Italia, Milan, 2009. MR 2524089
- [33] B. C. FRY T. K. ROY T. W. SECOMB, Capillary recruitment in a theoretical model for blood flow regulation in heterogeneous microvessel networks. *Physiol. Rep.* **1** (2013), no. 3, article no. e00050.

- [34] L. Fusi A. Farina, Linear stability analysis of blood flow in small vessels. *Appl. Eng. Sci.* 1 (2020), article no. 100002.
- [35] L. Fusi A. Farina, Flow stability of suspensions. Appl. Math. Comput. 410 (2021), article no. 126466. Zbl 1510.76054 MR 4281786
- [36] P. Gaehtgens, Flow of blood through narrow capillaries: rheological mechanisms determining capillary hematocrit and apparent viscosity. *Biorheology* **17** (1980), 183–189.
- [37] P. GAEHTGENS K. H. ALBRECHT F. KREUTZ, Fåhræus effect and cell screening during tub flow of human blood. I. Effect of variation of flow rate. *Biorheology* **15** (1978), 147–154.
- [38] P. Gaehtgens F. Kreutz K. H. Albrecht, Fahraeus effect and cell screening during tube flow of human blood. II. Effect of dextran-induced cell aggregation. *Biorheology* **15** (1978), 155–161.
- [39] O. R. GLIAH, In vitro investigation of cell-free layer formation in microchannels: Dependency on the red blood cell aggregation and field of shear. Ph.D. thesis, Faculty of Engineering, University of Ottawa, 2018.
- [40] H. L. GOLDSMITH G. R. COKELET P. GAEHTGENS, Robin Fåhræus: evolution of his concepts in cardiovascular physiology. *Am. J. Physiol.* **257** (1989), H1005–H1015.
- [41] R. J. Gratton R. E. Gandley J. F. McCarthy M. K. McLaughlin, Reduced vasomotion may contribute to the decrease in vascular resistance during pregnancy. *J. Soc. Gynecol. Investig.* **3** (1996), no. 2, 99A.
- [42] R. J. Gratton R. E. Gandley J. F. McCarthy W. K. Michaluk B. K. Slinker M. K. McLaughlin, Contribution of vasomotion to vascular resistance: a comparison of arteries from virgin and pregnant rats. *J Appl Physiol* **85** (1998), no. 6, 2255–2260.
- [43] S. Guadagni A. Farina, Entrance flow of a suspension and particles migration towards the vessel center. *Int. J. Non Linear. Mech.* **126** (2020), article no. 103587.
- [44] R. Gupta A. Kumar M. Singhal, A critical review of multiphase modelling of blood flow in human cardiovascular system. *J. Indian. Inst. Sci.* **104** (2024), 39–63.
- [45] E. Hatschek, Eine Reihe von abnormen Liesegang'schen Schichtungen. *Kolloid-Zeitschrift* **27** (1920), 225–229.
- [46] R. H. Haynes, Physical basis of the dependence of blood viscosity on tube radius. *Am. J. Physiol.* **198** (1960), 1193–1200.
- [47] M. Intaglietta, Vasomotion and flowmotion: physiological mechanisms and clinical evidence. *Vascular Medicine Review* vmr-1 (1990), no. 2, 101–112.
- [48] G. B. Jeffery, The motion of ellipsoidal particles immersed in a viscous fluid. *Proc. Roy. Soc. Lond. Ser. A* **102** (1922), 161–179. Zbl 49.0748.02
- [49] R. J. Jendrucko J. S. Lee, The measurement of hematocrit of blood flowing in glass capillaries by microphotometry. *Microvasc. Res.* **6** (1973), no. 3, 316–331.

- [50] T. W. Jones, Discovery that the veins of the bat's wing (which are furnished with valves) are endowed with rythmical contractility, and that the onward flow of blood is accelerated by each contraction. *Philos. Trans. R. Soc. Lond.* **142** (1852), 131–136.
- [51] N. Kikuchi J. T. Oden, Contact problems in elasticity: A study of variational inequalities and finite element methods. SIAM Stud. Appl. Math. 8, Society for Industrial and Applied Mathematics (SIAM), Philadelphia, PA, 1988. MR 961258
- [52] S. KIM R. L. KONG A. S. POPEL M. INTAGLIETTA P. C. JOHNSON, Temporal and spatial variations of cell-free layer width in arterioles. *Am. J. Physiol. Heart Circ. Physiol.* **293** (2007), no. 3, H1526–H1535.
- [53] M. Koenigsberger R. Sauser J. L. Bény J. J. Meister, Effects of arterial wall stress on vasomotion. *Biophys J* **91** (2006), no. 5, 1663–1674.
- [54] I. M. KRIEGER T. J. DOUGHERTY, A mechanism for non-Newtonian flow in suspensions of rigid spheres. *Trans. Soc. Rheology* 3 (1960), 137–152. Zbl 0100.21502
- [55] K. Kümin, Bestimmung des Zähigkeitskoeffizienten μ' für Rinderblut bei Newton'schen Strömungen in verschieden weiten Röhren und kapillaren bei physiologischer Temperatur. Inaugural-Dissertation, Universität Bern, 1949.
- [56] D. Lapi M. Di Maro T. Mastantuono N. Starita M. Ursino A. Colantuoni, Arterial network geometric characteristics and regulation of capillary blood flow in hamster skeletal muscle microcirculation. *Front. Physiol.* **9** (2019), 1953.
- [57] R. LIU X. WANG S. HOSHI Y. ZHANG, High-speed measurement of retinal arterial blood flow in the living human eye with adaptive optics ophthalmoscopy. *Opt. Lett.* **48** (2023), no. 8, 1994–1997.
- [58] P. Martini A. Pierach E. Scheryer, Die Strömung des Blutes in engen Gefäßen. Eine Abweichung vom Poiseuille'schen Gesetz. *Dtsch. Arch. Klin. Med.* **169** (1930), 212–222.
- [59] G. McHedlishvili, Basic factors determining the hemorheological disorders in the microcirculation. *Clin. Hemorheol. Microcirc.* **30** (2004), no. 3–4, 179–180.
- [60] C. Meyer G. de Vries S. T. Davidge D. C. Mayes, Reassessing the mathematical modeling of the contribution of vasomotion to vascular resistance. *J Appl Physiol* **92** (2002), no. 2, 888–889.
- [61] J. U. MEYER P. BORGSTRÖM L. LINDBOM M. INTAGLIETTA, Vasomotion patterns in skeletal muscle arterioles during changes in arterial pressure. *Microvasc. Res.* **35** (1988), no. 2, 193–203.
- [62] T. M. Mubita L. R. Rojas-Solórzano J. B. Moreno, A multiphase approach to model blood flow in micro-tubes. In Computational and experimental fluid mechanics with applications to physics, engineering and the environment, edited by L. Sigalotti, J. Klapp and E. Sira, pp. 235–247, Environ. Sci. Eng., Springer, Cham, 2014.
- [63] Y. Nubar, Effect of slip on the rheology of a composite fluid: application to blood. *Biorheology* **4** (1967), no. 4, 133–150.

- [64] A. R. Pries D. Neuhaus P. Gaehtgens, Blood viscosity in tube flow: dependence on diameter and hematocrit. *Am. J. Physiol.* **263** (1992), H1770–H1778.
- [65] A. R. Pries T. W. Secomb P. Gaehtgens, Biophysical aspects of blood flow in the microvasculature. *Cardiovasc. Res.* **32** (1996), no. 4, 654–667.
- [66] A. Quarteroni L. Formaggia, Mathematical modelling and numerical simulation of the cardiovascular system. In *Handbook of numerical analysis*. Vol. XII, pp. 3–127, North-Holland, Amsterdam, 2004. MR 2087609
- [67] A. Quarteroni C. Vergara, Computational models for hemodynamics. In *Encyclopedia of continuum mechanics*, edited by H. Altenbach and A. Öchsner, pp. 370–378, Springer, Berlin, 2020.
- [68] N. K. RAJEEVA PANDIAN A. JAIN, In silico analyses of blood flow and oxygen transport in human micro-veins and valves. *Clin. Hemorheol. Microcirc.* **81** (2022), no. 1, 81–96.
- [69] J. J. Reho X. Zheng S. A. Fisher, Smooth muscle contractile diversity in the control of regional circulations. *Am. J. Physiol. Heart Circ. Physiol.* **306** (2014), no. 2, H163–H172.
- [70] R. J. Roselli K. R. Diller, *Biotransport: principles and applications*. Springer, New York, 2011.
- [71] H. E. SALMAN H. C. YALCIN, Computational modeling of blood flow hemodynamics for biomechanical investigation of cardiac development and disease. J. Cardiovasc. Dev. Dis. 8 (2021), no. 2, article no. 14.
- [72] Т. W. Secomb, Blood flow in the microcirculation. In *Annual review of fluid mechanics*. *Vol. 49*, pp. 443–461, Annu. Rev. Fluid Mech. 49, Annual Reviews, Palo Alto, CA, 2017. Zbl 1359.76355 MR 3726586
- [73] M. Sharan A. S. Popel, A two-phase model for flow of blood in narrow tubes with increased effective viscosity near the wall. *Biorheology* **38** (2001), no. 5–6, 415–428.
- [74] Y. G. Stergiou A. T. Keramydas A. D. Anastasiou A. A. Mouza S. V. Paras, Experimental and numerical study of blood flow in μ-vessels: Influence of the Fåhræus–Lindqvist effect. *Fluids* 4 (2019), no. 3, article no. 143.
- [75] V. VAND, Viscosity of solutions and suspensions. I. Theory. J. Phys. Colloid. Chem. 52 (1948), no. 2, 277–299.
- [76] L. Wang et al., Vessel sampling and blood flow velocity distribution with vessel diameter for characterizing the human bulbar conjunctival microvasculature. Eye Contact Lens 42 (2016), no. 2, 135–140.
- [77] M. P. Wiedeman, Effect of venous flow on frequency of venous vasomotion in the bat wing. *Circ. Res.* **5** (1957), no. 6, 641–644.
- [78] T. Yamaguchi et al., Particle-based methods for multiscale modeling of blood flow in the circulation and in devices: challenges and future directions. Sixth International Bio-Fluid Mechanics Symposium and Workshop March 28–30, 2008 Pasadena, California. Ann. Biomed. Eng. 38 (2010), no. 3, 1225–1235.

[79] E. P. ZILOW – O. LINDERKAMP, Viscosity reduction of red blood cells from preterm and full-term neonates and adults in narrow tubes (Fåhræus–Lindqvist effect). *Pediatr Res.* **25** (1989), no. 6, 595–599.

Received 21 October 2024, and in revised form 16 November 2024

Angiolo Farina (corresponding author)
Dipartimento di Matematica e Informatica *Ulisse Dini*, Università di Firenze Viale G. B. Morgagni, 67a, 50134 Firenze, Italy angiolo.farina@unifi.it

Antonio Fasano Fiab SpA Via Bruno Passerini, 2, 50039 Vicchio (Firenze), Italy a.fasano@fiab.it

Fabio Rosso Dipartimento di Matematica e Informatica *Ulisse Dini*, Università di Firenze Viale G. B. Morgagni, 50134 Firenze, Italy fabio.rosso@unifi.it